Role of the Kelvin-Helmholtz instability in the evolution of magnetized relativistic sheared plasma flows

Nathaniel D. Hamlin*
Department of Physics and Astronomy, University of California, Los Angeles, California 90095, USA

William I. Newman†
Departments of Earth and Space Sciences, Physics and Astronomy, and Mathematics, University of California, Los Angeles, California 90095, USA

(Received 30 November 2012; revised manuscript received 11 March 2013; published 4 April 2013)

We explore, via analytical and numerical methods, the Kelvin-Helmholtz (KH) instability in relativistic magnetized plasmas, with applications to astrophysical jets. We solve the single-fluid relativistic magnetohydrodynamic (RMHD) equations in conservative form using a scheme which is fourth order in space and time. To recover the primitive RMHD variables, we use a highly accurate, rapidly convergent algorithm which improves upon such schemes as the Newton-Raphson method. Although the exact RMHD equations are marginally stable, numerical discretization renders them unstable. We include numerical viscosity to restore numerical stability. In relativistic flows, diffusion can lead to a mathematical anomaly associated with frame transformations. However, in our KH studies, we remain in the rest frame of the system, and therefore do not encounter this anomaly. We use a two-dimensional slab geometry with periodic boundary conditions in both directions. The initial unperturbed velocity peaks along the central axis and vanishes asymptotically at the transverse boundaries. Remaining unperturbed quantities are uniform, with a flow-aligned unperturbed magnetic field. The early evolution in the nonlinear regime corresponds to the formation of counter-rotating vortices, connected by filaments, which persist in the absence of a magnetic field. A magnetic field inhibits the vortices through a series of stages, namely, field amplification, vortex disruption, turbulent breakdown, and an approach to a flow-aligned equilibrium configuration. Similar stages have been discussed in MHD literature. We examine how and to what extent these stages manifest in RMHD for a set of representative field strengths. To characterize field strength, we define a relativistic extension of the Alfvénic Mach number M_A. We observe close complementarity between flow and magnetic field behavior. Weaker fields exhibit more vortex rotation, magnetic reconnection, jet broadening, and intermediate turbulence. Sufficiently strong fields ($M_A < 6$) completely suppress vortex formation. Maximum jet deceleration, and viscous dissipation, occur for intermediate vortex-disruptive fields, while electromagnetic energy is maximized for the strongest fields which allow vortex formation. Highly relativistic flows destabilize the system, supporting modes with near-maximum growth at smaller wavelengths than the shear width of the velocity. This helps to explain early numerical breakdown of highly relativistic simulations using numerical viscosity, a long-standing problem. While magnetic fields generally stabilize the system, we have identified many features of the complex and turbulent reorganization that occur for sufficiently weak fields in RMHD flows, and have described the transition from disruptive to stabilizing fields at $M_A \approx 6$. Our results are qualitatively similar to observations of numerous jets, including M87, whose knots may exhibit vortex-like behavior. Furthermore, in both the linear and nonlinear analyses, we have successfully unified the HD, MHD, RHD, and RMHD regimes.

DOI: 10.1103/PhysRevE.87.043101 PACS number(s): 52.27.Aj, 47.20.Ft, 52.27.Ny, 52.25.Xz

I. INTRODUCTION

The Kelvin-Helmholtz (KH) instability arises when a perturbation is applied to a flow that exhibits a transverse (shear) variation in flow speed, either continuous or discontinuous. The KH instability was discovered independently by Lord Kelvin in 1871 and by Helmholtz in 1868. Helmholtz [1] provided a qualitative discussion of the interaction between two vertically stratified fluids having different densities. Kelvin [2] studied this instability in the geophysical context of wind-water interactions or, more generally, a fluid and an air current in relative motion. This problem was further illuminated by Munk [3], who found a critical wind velocity of 6.5 m/s above which white caps suddenly emerge. An experimental demonstration of the KH instability was provided by Francis [4] for an air-oil interface. This has been extended to the problem of vertical stratification of air currents in the Earth's atmosphere, e.g., Chandrasekhar [5], Case [6], Dyson [7], Drazin [8], Drazin and Howard [9]. There have been many more recent studies of interactions between atmospheric air currents, e.g., Maslowe [10] and Swaters [11].

The KH instability has also been widely studied in many areas of astrophysical interest, including astrophysical jets, and interactions within the Earth's magnetosphere, e.g., Pu and Kivelson [12], Kivelson and Pu [13], Otto and Fairfield [14], and Faganello *et al.* [15]. Comparisons between jet observations and simulations have suggested that the KH instability may play an important role in jet morphology, including vortices, helical structures, filamentary features, etc. [16–20]. Apparent superluminal motion (i.e., behavior that gives the appearance of being greater than the speed of light, but is an effect of phase velocity), and relativistic boosting,

*nhamlin@physics.ucla.edu
†win@ucla.edu

demonstrate that many of these jets have highly relativistic flows [21], while the presence of magnetic fields is strongly supported by the commonly accepted model for jet formation from active supermassive black holes [22–24]. Relativistic boosting refers to large increases in observed spatial and temporal frequencies originating from sources whose speeds are comparable to the speed of light.

It is therefore of great interest to numerically simulate the KH instability in relativistic magnetized jets. However, the assumptions of relativity and magnetization greatly complicate the conservative equations used in simulations and, until 2006, the growth of the KH instability had not been accurately simulated in the RMHD regime, according to Bucciantini and Del Zanna [25]. This is largely due to the difficulty of recovering the primitive relativistic magnetohydrodynamic (RMHD) variables mass density, velocity, and pressure from the derived conserved mass, momentum, and energy densities, which must be done at each time step of a simulation. Unlike their nonrelativistic counterparts, the RMHD equations can not be inverted algebraically, and therefore require a numerical relaxation scheme. Our study uses a scheme developed by Newman [26], which is considerably more accurate and rapidly convergent than previous such schemes, such as the Newton-Raphson method, and is described briefly in Appendix B.

Many studies have explored the evolution of the KH instability in the MHD regime, and have identified various stages of nonlinear vortex inhibition by a magnetic field [14,27–29]. However, for the reasons mentioned above, this phenomenon has not been extensively studied in the RMHD regime. By overcoming the aforementioned difficulties of recovering the primitive RMHD variables from the conserved quantities, we have studied the nonlinear evolution of the KH instability in RMHD for a set of representative field strengths. In particular, for each field strength, we have examined in detail the manner and extent of manifestation of various stages of vortex inhibition. We have identified a class of bifurcations, which is to say, energy-transfer processes (viscous dissipation, maximization of electromagnetic energy) which are optimized for intermediate field strengths. We have also described the complexity of turbulent reorganization associated with the broad regime of vortex-disruptive fields, and demonstrated convergence in nonlinear evolution between strongly vortex-disruptive and vortex-suppressing fields. Some MHD studies (e.g., Baty *et al*. [29]) have used the Alfvénic Mach number to characterize the strength of the magnetic field. We have demonstrated that within a regime of moderately relativistic flow speeds, the influence of a magnetic field in RMHD is correlated with a suitably defined relativistic extension of the Alfvénic Mach number. Finally, we have identified potential comparisons of our results to various astrophysical jets, and have unified the HD, MHD, RHD, and RMHD regimes in both linear and nonlinear analyses.

It should be noted that throughout this paper when we refer to "unperturbed" quantities, we mean the initial value or distribution of a quantity prior to perturbing the system in an eigenmode. Also, we frequently refer to the "deceleration" of the flow as the simulation progresses. The maximum and average flow speeds both decrease over time. However, the relativistic momentum, given in Sec. IV, is still conserved. The relativistic momentum depends not only on velocity, but also on such quantities as density and pressure, the average values of which increase over time, as we will see in Sec. VIII G. Having provided a motivation for our research, we now proceed with a survey of some of the salient literature on the KH instability and its role in the modeling of astrophysical jets.

II. PRIOR RESEARCH

Here, we survey some of the previous research of the KH instability. The KH instability has been explored extensively in the hydrodynamic (HD), relativistic hydrodynamic (RHD), and magnetohydrodynamic (MHD) regimes in both linear and nonlinear analyses. Linear analyses have also been performed in the relativistic magnetohydrodynamic (RMHD) regime. The KH instability has been applied to astrophysical jets in the HD, RHD, and MHD regimes. Recent numerical advances have allowed for general modeling of these jets in RMHD. However, owing to the aforementioned numerical difficulty of recovering the primitive RMHD variables from the conserved quantities, there are not many detailed numerical studies of the nonlinear development of the KH instability in RMHD plasma flows, with potential applications to astrophysical jets. Following, we summarize the salient features of the different areas of research mentioned above.

Chandrasekhar [5] derived an expression for the growth rate of the KH instability for two incompressible magnetohydrodynamic (MHD) fluids separated by a tangential discontinuity (TD). Let the fluids have unperturbed densities ρ_1 and ρ_2, unperturbed flow velocities v_{z1} and v_{z2}, and unperturbed magnetic fields $\mathbf{B}_1$ and $\mathbf{B}_2$. When the flow is perturbed by a disturbance with wave vector $\mathbf{k}$, the resulting growth rate is

$$\omega_i = \sqrt{\frac{\rho_1\rho_2 k_z^2 (v_{z2}-v_{z1})^2}{(\rho_1+\rho_2)^2} - \frac{(\mathbf{k}\cdot\mathbf{B}_1)^2+(\mathbf{k}\cdot\mathbf{B}_2)^2}{4\pi(\rho_1+\rho_2)}}. \qquad (1)$$

This expression tells us that the magnetic field reduces the growth rate of the instability and, in this sense, is analogous to surface tension stabilizing the surface of the ocean to disturbances caused by wind. In order for the perturbation to grow, its wave vector must perform work to bend the field lines, and this work is proportional to the inner products with the fields, shown above. There is also a minimum velocity difference in order for instability, which is larger for larger field strengths. Beyond this threshold, the growth rate increases with increasing relative velocity. An incompressible fluid has an effectively infinite sound speed. However, for a compressible fluid (which has finite sound speed) with a tangential discontinuity (TD), Pu and Kivelson [12] and Kivelson and Pu [13] showed that in addition to a lower-critical velocity difference for instability, there is also an upper-critical velocity difference, so that instability only occurs between these two critical values (for given fixed values of the other parameters). The lower-critical velocity difference, and growth rates at low flow speeds, are accurately predicted by the above expression for incompressible flows. Ferrari *et al*. [30] studied the KH instability for a TD in RMHD, considering cases in which the displacement current was neglected.

Bodo *et al*. [31] studied the KH instability with a TD in RHD, and found that for uniform unperturbed density and

pressure, and in a frame in which the flow velocities are equal and opposite, the dispersion relation can be solved analytically for the growth rate. They found that the stability criterion can be written in terms of a relativistic extension of the Mach number, which they defined as

$$M_{\rm rel} = \frac{v_{z0}\gamma}{c_s\gamma_s}, \quad \text{where}$$
$$\gamma = \frac{1}{\sqrt{1 - v_{z0}^2/c^2}}, \quad \gamma_s = \frac{1}{\sqrt{1 - c_s^2/c^2}}, \tag{2}$$

where v_{z0} and $-v_{z0}$ are the equal and opposite flow speeds, c_s is the relativistic sound speed, and γ and γ_s are the respective Lorentz factors. Bodo *et al*. [31] found that for flow-aligned perturbations, the KH instability is suppressed when $M_{\rm rel} > \sqrt{2}$. This is analogous to the HD case, for which the system is stabilized to these perturbations when the nonrelativistic Mach number v_{z0}/c_s is larger than $\sqrt{2}$. For purposes of comparison with our study, the more relevant frame is that in which one of the fluids is stationary (i.e., the ambient medium), and one fluid moves at a velocity u_{z0} with respect to the other, where

$$u_{z0} = \frac{2v_{z0}}{1 + v_{z0}^2/c^2}. \tag{3}$$

We can define $M_{u,\rm rel}$ in terms of u_{z0} in the same manner that we define $M_{\rm rel}$ in terms of v_{z0}, and we find that instability to flow-aligned perturbations is suppressed at all sound speeds when $M_{u,\rm rel} > 4$. We will see in Sec. VI that when the TD is replaced by a shear variation, instability to flow-aligned perturbations extends to much higher Mach numbers than this.

Linear analyses of the KH instability, in the presence of a continuous velocity shear instead of a TD, were performed in HD by Blumen [32], Blumen *et al*. [33], and Ray [34], among others, in RHD by Birkinshaw [35], among others, and in MHD by Miura and Pritchett [36], Kivelson and Pu [13], and Choudhury and Lovelace [37], among others. These studies have identified several differences between a TD and a velocity shear. The first is the dependence of growth rate on wave number. In the case of a TD, the growth rate increases linearly with wave number. In the case of a velocity shear, there is generally a wave number corresponding to maximum growth, and a larger wave number above which the system is stabilized (corresponding to a wavelength which is roughly equal to the width of shear variation). The second difference is that instability to a given perturbation orientation can extend to much higher Mach numbers than is the case for a TD. We will observe these properties in Sec. VI, along with further destabilization due to highly relativistic flow speeds.

Nonlinear simulations of the KH instability have been performed in MHD by Malagoli *et al*. [38], Frank *et al*. [27], Keppens *et al*. [39], Ryu *et al*. [28], Otto and Fairfield [14], Baty *et al*. [29], Faganello *et al*. [15], among others. These studies have frequently identified vortex formation in the early nonlinear regime, followed by field-induced vortex disruption, magnetic reconnection, turbulent breakdown, and relaxation to an equilibrium state. We examine in detail how and to what extent these stages manifest in RMHD for a set of representative field strengths.

The KH instability has often been invoked in the modeling of extragalactic astrophysical jets. Bicknell and Begelman [20] used the KH instability to interpret the structure of the radio jet M87. Hardee [17,18] used the KH instability to model the ribbons and threads in the jet 3C 120. Lobanov and Zensus [19] used the KH instability to model the cosmic double helix in the jet 3C 273. These studies strongly suggest that the KH instability plays an important role in jet development. General modeling of jet evolution has been performed in RHD by such authors as Duncan and Hughes [40] and Marti *et al*. [41], and more recently in RMHD by such authors as Koide *et al*. [42], Leismann *et al*. [43], and Mignone *et al*. [44]. These RMHD studies have improved due to numerical advances which improve the accuracy and precision with which the primitive variables can be recovered from the conserved quantities in the single-fluid RMHD equations. However, these RMHD studies have not focused on the role of the KH instability with the level of detail that we examine in our study. Although our study focuses on the physics governing the nonlinear development of a sheared plasma flow in RMHD, our results have potential applications to numerous astrophysical jets. Furthermore, in both our linear and nonlinear analyses of this problem, we have unified the behavior in the HD, MHD, RHD, and RMHD regimes.

We have discussed the manner in which our study builds upon existing research. We now present the physical model of our system.

III. PHYSICAL MODEL

Here, we discuss the assumptions involved in the model of our system. The fluid in this study is relativistic, magnetized, and hydrodynamic (RMHD). The fluid is also compressible, infinitely conducting, adiabatic, and has an isotropic pressure tensor. These are the assumptions made in most single-fluid MHD and RMHD studies [14,27,28,36,38], including those that involve simulations of jets [40,42,44].

We assume a two-dimensional slab geometry in the x-z plane, where z is the flow direction and x the shear direction. The unperturbed pressure and density are uniform. The unperturbed magnetic field is uniform and aligned with the flow direction (the z direction). The unperturbed velocity has the "Bickley jet" shear variation [45]

$$v_z(x) = v_{z0}\,\mathrm{sech}^2(x/r_0). \tag{4}$$

This profile, also sometimes referred to as the "sech-squared" velocity profile, has the appearance of a Gaussian profile, vanishing asymptotically at the exterior boundaries, peaking in the center, and symmetric about the center. The boundary conditions are periodic in the x and z directions. Thus far, the Bickley jet has been used in meteorological and oceanographic studies of incompressible, nonrelativistic, unmagnetized fluids. Bickley [45] originally derived this profile as a solution to the Prandtl boundary layer equations (i.e., the HD single-fluid equations in the presence of a viscous boundary layer). Savic [46] used the Bickley jet to model vortex motion in gaseous jets. This profile was also used by Lipps [47] to study the stability of mid-latitude atmospheric jets, by Stern [48] to study oceanic thermocline jets (the "thermocline" layer is the depth corresponding to the largest

temperature gradient), and to examine wakes behind large obstacles, as done by Mattingly and Criminale [49]. The Bickley jet has been used in meteorological studies by Howard and Drazin [50], Maslowe [10], and Swaters [11], among others.

However, the salient research of the Kelvin-Helmholtz instability, as it applies to compressible, magnetized, or relativistic fluids, has not thus far used a Bickley jet profile, nor has it been applied to astrophysical jets. Rather, prior studies have often used a slab geometry with a single transition layer between jet and ambient medium [14,27,36,38], typically a hyperbolic tangent profile. Other studies have used a cylindrical geometry [18,41–44], which allows for a more complete exploration of the jet cross section. However, the RMHD cylindrical studies tend to focus on more general aspects of jet evolution, rather than the specific role of the KH instability. This is largely due to the many numerical difficulties that arise when the RMHD conservation-diffusion equations are modeled in cylindrical geometry in the presence of a velocity shear. By allowing for the use of a slab geometry, the Bickley jet profile avoids many of these difficulties, while spanning an entire cross section of the jet, and providing a built-in mechanism for validating the numerical accuracy of the solutions by ascertaining that certain symmetry properties are preserved throughout the evolution. One example is a condition on the vorticity, i.e., the curl of the velocity.

Having discussed the basic properties of our plasma flow, we now present the single-fluid RMHD equations that govern its evolution.

IV. EQUATIONS

We use the single-fluid RMHD equations of Anile [51] in conservative form. Let ρ, P, and w denote the density, pressure, and enthalpy, respectively, in the proper frame of the fluid, which has adiabatic index Γ. Then, we have

$$w = \rho c^2 + \frac{\Gamma P}{\Gamma - 1}. \tag{5}$$

Let $\beta = \mathbf{v}/c$ denote the fluid velocity, and $\gamma = (1-\beta^2)^{-1/2}$ the Lorentz factor. Let $\mathbf{B}$ denote the magnetic field in the stationary frame. Then, we define the covariant velocity u^μ and covariant magnetic field b^μ according to

$$\begin{aligned} u^\mu &= \gamma(1,\beta), \quad b^0 = \gamma(\beta\cdot\mathbf{B}), \\ b^i &= \frac{B^i + \gamma^2(\beta\cdot\mathbf{B})\beta^i}{\gamma}. \end{aligned} \tag{6}$$

The governing single-fluid equations are given by

$$\frac{\partial}{\partial x^\mu}\eta^\mu = 0, \quad \frac{\partial}{\partial x^\mu}\tau^{\mu\nu} = 0, \quad \frac{\partial}{\partial x^\mu}\mathcal{G}^{\mu\nu} = 0, \tag{7}$$

where

$$\begin{aligned} \eta^\mu &= \rho u^\mu, \quad \tau^{\mu\nu} = (w+b^2)u^\mu u^\nu + \left(P + \frac{b^2}{2}\right)g^{\mu\nu} - b^\mu b^\nu, \\ \mathcal{G}^{\mu\nu} &= b^\mu u^\nu - b^\nu u^\mu, \quad x^\mu = (ct,\mathbf{r}). \end{aligned} \tag{8}$$

The first of Eqs. (7) describes mass transport. The time component of the second equation describes energy transport, while the spatial components of the second equation describe momentum transport. The time component of the third equation states that $\mathbf{B}$ has zero divergence, while the spatial components of the third equation constitute Faraday's law. This is the covariant version of the equations, which is used in the RMHD studies of Leismann *et al.* [43], Mignone *et al.* [44], Komissarov [52], Balsara [53], Mignone *et al.* [54], Zrake and MacFadyen [55], among others. In the nonrelativistic limit ($\gamma \to 1$, $\rho c^2 \gg P$), we recover the MHD single-fluid equations. In the unmagnetized limit ($b \to 0$), we recover the RHD equations. In the unmagnetized nonrelativistic limit, we recover the HD equations.

We have presented the equations that govern the evolution of a fluid in RMHD. We now apply these equations to our model. In the next section, we discuss how we linearize these equations in order to construct a numerical perturbation in which to launch our system at the start of a simulation.

V. CONSTRUCTING A NUMERICAL MODE

Here, we describe the method for launching the system in a numerical eigenmode. We linearize the RMHD equations (7) in the presence of the unperturbed velocity shear given by (4), and thereby derive the relations characterizing a linear mode of the KH instability in RMHD. We restrict our attention to the x-z plane, so that there are no components, nor is there any evolution, in the y direction. We consider a fluid which is compressible, adiabatic, isotropic, and infinitely conducting. The fluid has a uniform unperturbed density ρ_0, a uniform unperturbed pressure P_0, and flows in the z direction with some unperturbed velocity profile $v_{z0}(x)$, where x is the direction transverse, or shear, to the flow. The fluid is immersed in a uniform unperturbed magnetic field $\mathbf{B}_0 = B_{z0}\hat{z}$ aligned with the flow direction. This is the equilibrium situation. We then perturb the fluid with a perturbation aligned with the flow, having wave number k_z. In the linear regime, the system can be described by

$$\begin{aligned} \rho(x,z,t) &= \rho_0 + \delta\rho(x)\exp[i(k_z z - \omega t)], \\ P(x,z,t) &= P_0 + \delta P(x)\exp[i(k_z z - \omega t)], \\ v_x(x,z,t) &= \delta v_x(x)\exp[i(k_z z - \omega t)], \\ v_z(x,z,t) &= v_{z0}(x) + \delta v_z(x)\exp[i(k_z z - \omega t)], \\ B_x(x,z,t) &= \delta B_x(x)\exp[i(k_z z - \omega t)], \\ B_z(x,z,t) &= B_{z0} + \delta B_z(x)\exp[i(k_z z - \omega t)]. \end{aligned} \tag{9}$$

When these linearized forms are inserted into Eqs. (7), we obtain a second-order ordinary differential equation (ODE) in the perturbation to the total pressure (magnetic plus thermal), which we denote δP_b:

$$\Omega^2(x)\frac{d}{dx}\left[\frac{1}{\Omega^2(x)}\frac{d\delta P_b}{dx}\right] + k_x^2(x)\delta P_b(x) = 0, \tag{10}$$

where

$$\begin{aligned} \delta P_b(x) &= \delta P(x) + \mathbf{B}_0\cdot\delta\mathbf{B}, \quad \text{total pressure}, \\ \Omega^2(x) &= \gamma(x)^2\bar{\omega}(x)^2 - v_{Az}^2\left(k_z^2 - \frac{\omega^2}{c^2}\right), \\ k_x^2(x) &= \frac{\gamma(x)^2\bar{\omega}(x)^2 k_d(x)^2 - \omega_d(x)^2\left(k_z^2 - \omega^2/c^2\right)}{\gamma(x)^2\bar{\omega}(x)^2 + \omega_d(x)^2}, \end{aligned}$$

$$\begin{aligned}
\omega_d(x)^2 &= \gamma(x)^2 v_{Az}^2 \left(\frac{\bar{\omega}(x)^2}{c_s^2} - \bar{k}_z(x)^2 \right), \\
k_d(x)^2 &= \gamma(x)^2 \left(\frac{\bar{\omega}(x)^2}{c_s^2} - \bar{k}_z(x)^2 \right), \\
\bar{\omega}(x) &= \omega - k_z v_{z0}(x), \quad \bar{k}_z(x) = k_z - \frac{\omega v_{z0}(x)}{c^2}, \\
v_{Az} &= \frac{B_{z0}}{\sqrt{w_0}}, \quad \text{relativistic Alfvén speed}, \\
\gamma(x) &= \frac{1}{\sqrt{1 - v_{z0}(x)^2/c^2}}, \\
c_s^2 &= c^2 \frac{\Gamma P_0}{w_0}, \quad \text{relativistic sound speed}.
\end{aligned} \tag{11}$$

In the nonrelativistic limit of Eq. (10), we recover the MHD equation of Miura and Pritchett [36] and Lovelace *et al.* [56]. In the unmagnetized limit of (10), we recover the RHD equation of such papers as Bodo *et al.* [31] and Birkinshaw [35]. In the unmagnetized nonrelativistic limit of (10), we recover the HD equation of such papers as Blumen [32], Blumen *et al.* [33], and Ray [34]. An important observation is that in each of the four regimes (HD, RHD, MHD, and RMHD), the second-order ODE in the total pressure perturbation is given by (10), with suitable definitions of $\Omega^2(x)$ and $k_x^2(x)$.

We solve Eq. (10) using what is known as the shooting method, which is discussed in Hairer *et al.* [57] and also used in the shear layer study of Blumen [32]. We integrate inward from the outer boundaries, constructing left and right total pressure perturbation profiles, and perform the integration using a fourth-order Runge-Kutta method, as described, for example, in Ralston and Rabinowitz [58]. We require that the pressure perturbation, and its x derivative, both approximately vanish at the outer boundaries (the derivative vanishes exactly, while the pressure is initialized at a small nonzero value). The inward integration ensures that the physical solution prevails over the unphysical one. We repeat this process over an array of complex frequencies. The eigenfrequency is the frequency for which the left and right pressure profiles converge smoothly at a point near the center (near $x = 0$). Let ω denote this frequency. The corresponding complex perturbations are defined in terms of the linearized RMHD equations. The initial distribution of a quantity f is then the unperturbed value plus the real part of the perturbation:

$$f(x,z,0) = f_0 + \mathrm{Re}[\delta f(x) \exp(i k_z z)], \tag{12}$$

where f represents density, pressure, velocity components, or magnetic field components. For a given wave number k_z, there are multiple possible modes, i.e., multiple values of ω. We select the mode with the fastest growth rate, which in this case corresponds to antisymmetric profiles of the perturbations to pressure, longitudinal velocity, and longitudinal magnetic field, and symmetric profiles of the perturbations to transverse velocity and transverse magnetic field. These are labeled "sinuous" modes by Drazin and Howard [9]. The modes with the opposite symmetries are much more stable, i.e., have much lower growth rates, in our geometry. These are labeled "varicose" modes by Drazin and Howard [9]. We select for the fastest-growing sinuous mode. Both real and imaginary parts of each profile have the same symmetry. As a result, each transverse cross section of the perturbation distribution has the same symmetry (or antisymmetry), at all locations along the flow direction.

We have discussed our method for constructing a numerical eigenmode in which the system is launched at the start of the simulation. We now proceed, in the next section, to describe the stability properties of these modes.

VI. LINEAR STABILITY ANALYSIS

We now examine the KH-unstable region corresponding to the eigenmodes derived by the method described above, i.e., the eigenmodes corresponding to a "sech-squared" shear variation in the unperturbed velocity. We examine the dependence of growth rate and phase velocity first on flow speed, then on magnetic field strength, and finally on the wave number k_z of the initial perturbation. Throughout Secs. VI A and VI B, the wave number of the initial perturbation is $k_z = 0.8/r_0$, which is the value used in the simulations, and is approximately the value corresponding to maximum growth.

A. Dependence of growth rate on flow speed

Figure 1(a) displays growth rate (in units of c/r_0) as a function of flow speed for different values of the sound speed. There is no magnetic field. At all sound speeds, instability persists into the highly relativistic regime. As the sound speed increases, the growth rates increase. Figure 1(a) illustrates the stabilizing influence of a small sound speed (greater compressibility). Under these circumstances, the density is larger compared to the pressure, and the bulk flow therefore has more mechanical energy. This has a stabilizing effect, as it means that flow-aligned perturbations must perform a greater amount of work to deform the flow. Figure 1(b) displays the corresponding ratio of phase velocity to flow speed. This ratio increases as flow velocity increases. For smaller sound speeds, the phase velocity is larger. As flow speed increases or sound speed decreases, the phase velocity becomes more comparable to the flow speed. For a given set of parameters, we seek to recover the fastest-growing sinuous mode (i.e., modes with antisymmetric shear profiles of pressure perturbation). The varicose modes (symmetric shear profiles of pressure perturbation) generally have much smaller growth rates. However, at low flow speeds, the growth rate of the sinuous mode is very low, comparable to the growth rates of varicose modes, making it difficult for the search algorithm to distinguish between the sinuous and varicose modes. This gives rise to the spikes seen in Fig. 1(a), where the algorithm has recovered varicose modes instead of the intended sinuous mode.

In Fig. 2, we plot the (a) growth rate and (b) phase velocity for the same sound speeds, but this time as a function of the covariant velocity $u_{z0} = \gamma v_{z0}/c$, where $\gamma = (1 - v_{z0}^2/c^2)^{-1/2}$ is the Lorentz factor. Note that in the highly relativistic regime, the covariant velocity and Lorentz factor are approximately equal. Figure 2(a) illustrates that for any sound speed, the growth rate decreases with increasing flow speed in the highly relativistic regime. The most rapid decrease seems to occur for Lorentz factors ranging from about 2 to about 20, and the subsequent decrease is more gradual. Most of the curves exhibit a kink, or noticeable change in behavior, at around $\gamma =$

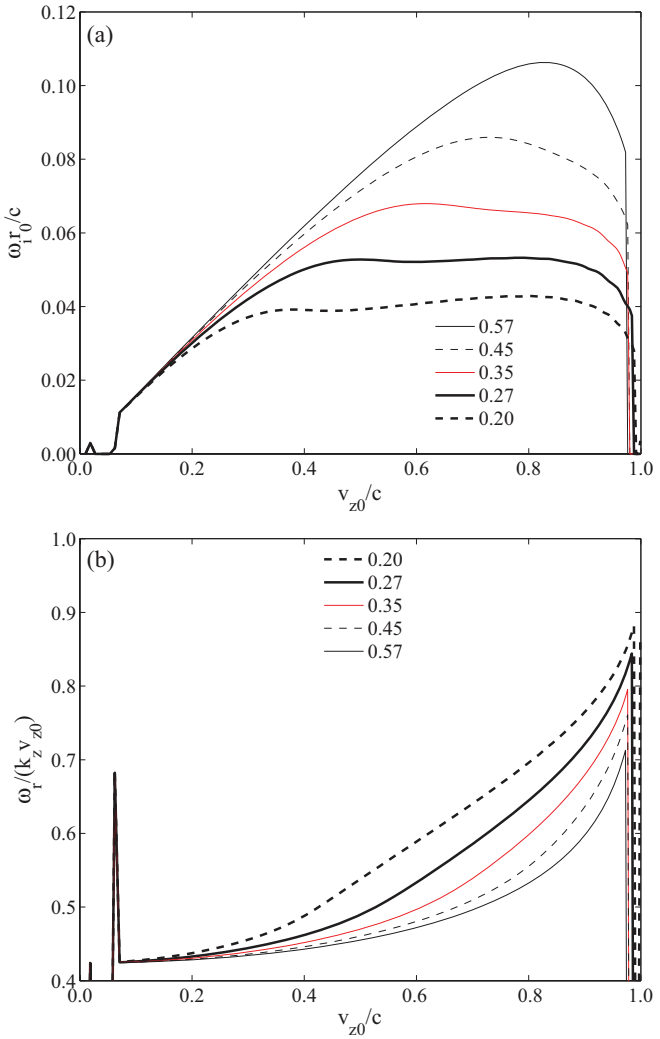

FIG. 1. (Color online) Growth rate and phase velocity vs flow speed at different sound speeds (RHD), where c_s/c is labeled above.

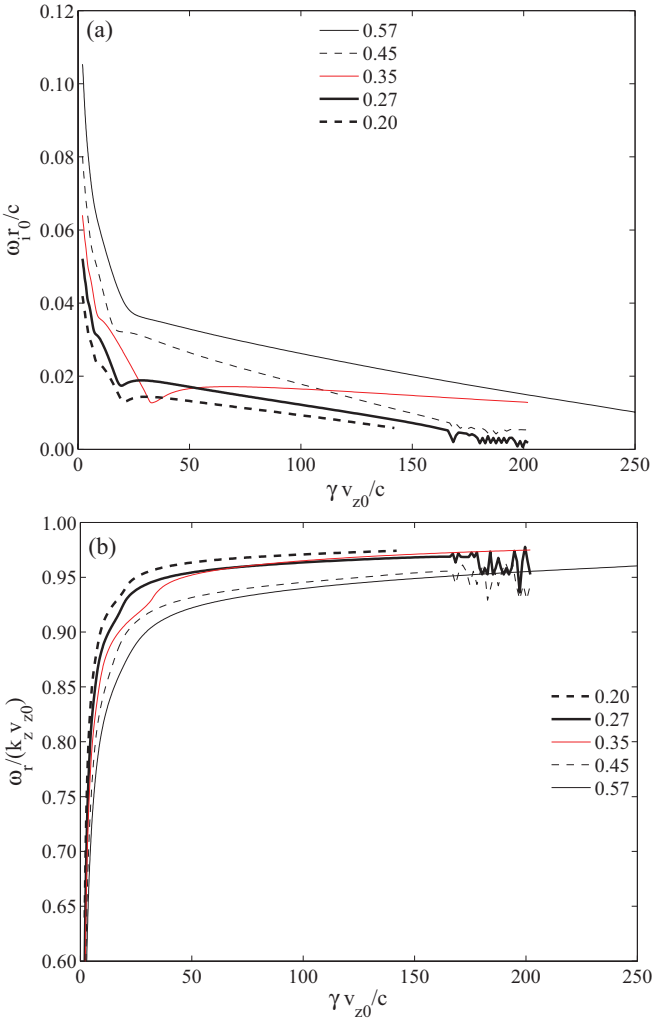

FIG. 2. (Color online) Growth rate and phase velocity vs $\gamma v_{z0}/c$ at different sound speeds (RHD), where c_s/c is labeled above.

20. This most likely corresponds to some sort of transition from sinuous modes (antisymmetric pressure profiles) to varicose modes (symmetric pressure profiles). That is, for flow speeds less than about $\gamma = 20$, the fastest-growing modes are sinuous, but Fig. 2(a) shows that this growth rate decreases rapidly from $\gamma = 2$ to about $\gamma = 20$. As shown in Fig. 2(b), this corresponds to a rapid increase in the sinuous phase velocity.

At about $\gamma = 20$, the growth rate of the sinuous mode drops below the growth rates of the varicose modes, which, for $\gamma < 20$, seem to have much less dependence on flow speed than the growth rate of the sinuous mode. For γ larger than roughly 20, the fastest-growing mode is now a varicose mode. For $c_s = 0.35\,c$, the transition in growth behavior occurs at a larger value of $\gamma \approx 33$, as shown by the red curve in Fig. 2(a). After the transition, the phase velocity of the varicose mode changes very little, as shown in Fig. 2(b). In particular, this figure shows that the ratio of phase velocity to flow speed seems to asymptotically approach unity as the flow speed approaches the speed of light (as the Lorentz factor goes to infinity). Figure 2 also shows that, even when the growth rate behavior is altered for highly relativistic flow speeds, the growth rates are still higher, and the phase velocities lower, for higher sound speeds, as we found for the less highly relativistic flow speeds shown in Fig. 1.

We see that in the highly relativistic regime, the system becomes more KH stable to perturbations with wave numbers on the order of $1/r_0$, which is the approximate wave number corresponding to maximum growth for moderately relativistic flow speeds less than about $0.85\,c$, as we will see in Fig. 4. However, we show in Sec. VI C that highly relativistic flow speeds can render the system less KH stable to perturbations with higher wave numbers, i.e., smaller wavelengths.

Figures 1 and 2 highlight an important difference between a tangential discontinuity and a shear variation in the velocity profile. Bodo *et al.* [31] demonstrated that for a tangential discontinuity, in the frame in which one of two adjacent flows is stationary, instability to flow-aligned perturbations is suppressed for relativistic Mach numbers larger than 4, for all sound speeds. In our case (a "sech-squared" shear variation), we see from Figs. 1 and 2 that there is no critical velocity or Mach number above which the system is KH stable to flow-aligned perturbations. Note that our two-dimensional system is restricted to flow-aligned perturbations.

In the next section, we examine the dependence of growth rate on the magnetic field strength.

B. Dependence of growth rate on magnetic field

A magnetic field has the effect of suppressing the KH instability. In the linear regime, the field reduces the growth rate of the eigenmode. We find that within a regime of moderately relativistic unperturbed flow speeds (between approximately $0.4\,c$ and $0.8\,c$ along the central axis), the fractional reduction in growth rate is closely correlated with a relativistic version of the Alfvénic Mach number, which we define as follows:

$$M_A = \frac{v_{z0}\,\gamma}{v_A\,\gamma_A} = \frac{v_{z0}}{v_A}\sqrt{\frac{1 - v_A^2/c^2}{1 - v_{z0}^2/c^2}}, \tag{13}$$

where v_{z0} is the amplitude of the unperturbed flow speed, v_A is the unperturbed Alfvén speed, and γ and γ_A are the Lorentz factors corresponding to the flow speed and Alfvén speed, respectively. Our definition of M_A is analogous to the manner in which Bodo *et al.* [31] defined a relativistic sonic Mach number. The correlation of growth rate with M_A is seen in Fig. 3, where the growth rate is plotted as a function of M_A^{-1} for each of several flow speeds. Specifically, the dependent variable is the ratio of the growth rate to its corresponding value in the unmagnetized case. The curves very closely overlay one another, and have a common instability threshold of $M_A^{-1} \approx \frac{1}{3}$. This correspondence, however, breaks down for $v_{z0} > 0.8\,c$. The correlation of growth rate with M_A is considerably closer for the pressure-dominated system [Fig. 3(a)] than for the density-dominated system [Fig. 3(b)]. This underscores the fundamental importance of the relativistic Alfvénic Mach number in characterizing the influence of the magnetic field on the development of a KH-unstable mode. This applies not only in the linear growth, but also the nonlinear evolution, as we will see in Sec. VIII, when we discuss the nonlinear results of our numerical simulations, and characterize field strength in terms of M_A rather than the plasma β or Alfvén speed. We will provide further elaboration on the correlation with M_A in Sec. VIII I. This result is a relativistic extension of the MHD study of the KH instability by Baty *et al.* [29], who identified a close correlation of magnetic field influence with a nonrelativistic Alfvénic Mach number.

In the next section, we examine the dependence of growth rate on the wave number k_z of the initial perturbation.

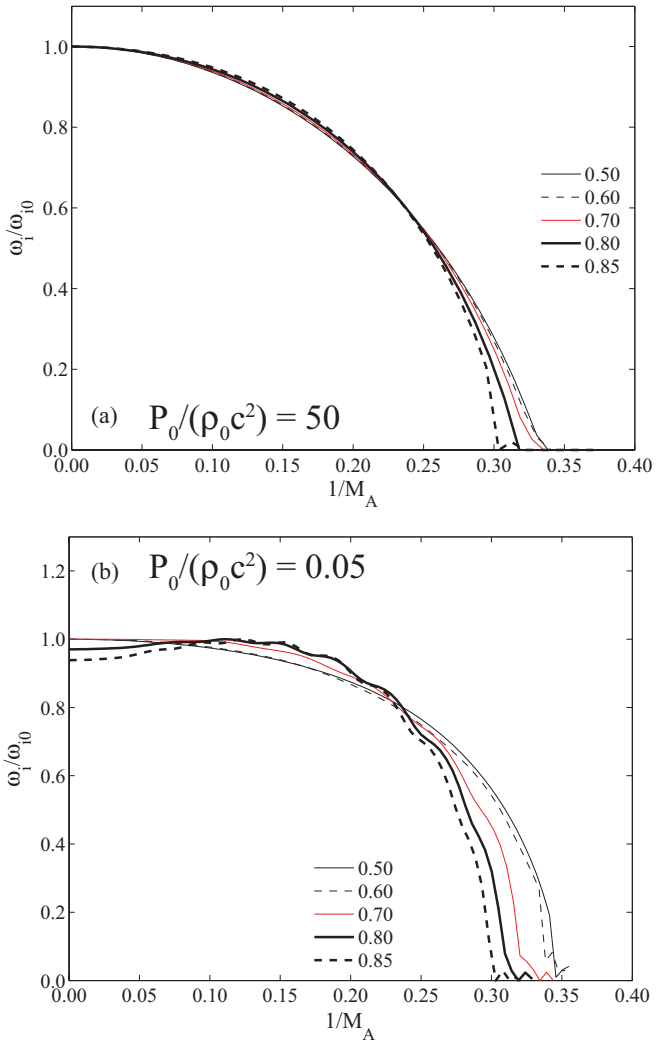

FIG. 3. (Color online) Growth rate vs M_A^{-1} at different flow speeds (RMHD), where v_{z0}/c is labeled above.

C. Dependence of growth rate on wave number

Figure 4 displays growth rate (in units of c/r_0) as a function of the wave number k_z (in units of $1/r_0$), again for several values of the flow speed. As with the HD case, the growth curve has a concave-downward shape, with a wave number corresponding to maximum growth and a larger wave number above which the system is stabilized. This wave number corresponds to a wavelength which is on the order of the width of shear variation (which in our model is half the initial jet width, or about $2\,r_0$). This is in contrast to the case of a step-function velocity profile considered earlier, for which the growth rate increases linearly with k_z. We see that with an increase in flow speed, there is an increase in the peak growth rate and in the range of instability. However, this trend breaks down for flow speeds larger than $0.8\,c$, and the maximum

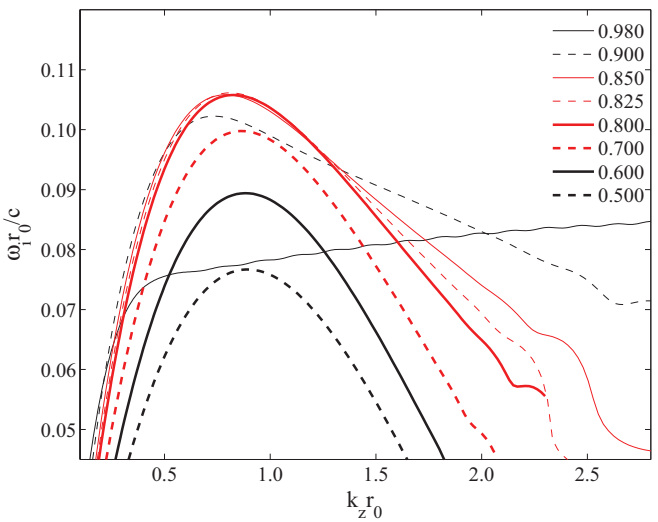

FIG. 4. (Color online) Growth rate vs k_z at different flow speeds (RHD), where v_{z0}/c is labeled above.

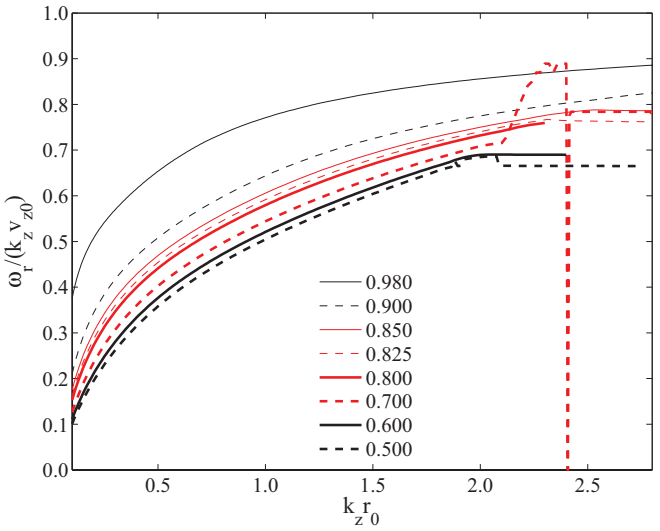

FIG. 5. (Color online) Phase velocity vs k_z at different flow speeds (RHD), where v_{z0}/c is labeled above.

growth rate is noticeably less at $0.9\,c$ than at $0.85\,c$. For flow speeds less than around $0.825\,c$, maximum growth occurs between $k_z = 0.8/r_0$ and $1/r_0$, and the growth curves have qualitatively similar concave-downward shapes. However, at $0.9\,c$, maximum growth occurs at roughly $k_z = 0.7/r_0$. As the flow speed becomes more relativistic, the growth rate decreases more slowly for larger k_z. At the highly relativistic flow speed of $0.98\,c$, the growth rates are somewhat lower, but growth rate no longer decreases with increasing k_z, and instead continues a gradual *increase*. At $0.98\,c$, the system is not stabilized until k_z exceeds approximately $5.36/r_0$, corresponding to a wavelength of $2\pi/k_z = 1.17\,r_0$, which is narrower than the width of shear variation ($\approx 2\,r_0$).

We see that the growth behavior is qualitatively different for highly relativistic flows. For such flows, the Lorentz factor is orders of magnitude larger, and this significantly modifies the terms in the fluid equations and in the second-order ODE to the pressure perturbation [Eq. (10)]. These terms are proportional to at least the second power of the Lorentz factor. At highly relativistic velocities, we have near-maximum growth at wavelengths smaller than the width of shear variation. This is one manifestation of the tendency of relativistic effects to destabilize the system, and a possible contributing factor to the numerical breakdown observed at Lorentz factors larger than about 2.

When we compare Figs. 4 and 5, we notice that at a given flow speed, there is a change in the behavior of the phase velocity when the corresponding growth curve drops to zero. Again, this is due to the presence, in the complex plane, of a family of varicose modes at low growth rates ($\omega_i < 0.01\,c/r_0$). Recall that the search algorithm attempts to recover the fastest-growing sinuous mode in each case. When the growth rate of this mode becomes too low, however, it becomes difficult to distinguish this mode from the varicose modes.

When we plot growth rate as a function of flow speed, we find that KH instability extends to much higher Mach numbers in our model (with velocity shear) than is the case for a tangential discontinuity, for which Bodo *et al.* [31] found that the system is stabilized to flow-aligned perturbations in RHD for Mach numbers larger than 4. Nonrelativistic versions of this result appear in such papers as Miura and Pritchett [36] and Ray [34]. In our examination of growth rate as a function of field strength, we find that the fractional reduction in growth rate is closely correlated with a relativistic version of the Alfvénic Mach number, which we define analogously to the manner in which Bodo *et al.* [31] defined a relativistic sonic Mach number. In our examination of growth rate as a function of perturbation wave number k_z, we find that for moderately relativistic flow speeds, there is a wave number corresponding to maximum growth, and a larger wave number above which the system is stabilized (corresponding to a wavelength which is on the order of the width in velocity shear). This is also the result for nonrelativistic systems. However, for highly relativistic flow speeds, we observe near-maximum growth at wavelengths which are smaller than the width of velocity shear. This is one manifestation of the destabilizing influence of relativistic flows, and may explain the early numerical breakdown of numerical viscosity simulations with Lorentz factors larger than roughly 2, a problem discussed by Marti and Muller [59].

We have discussed the properties of numerical eigenmodes in which we launch the system at the start of a simulation. We now discuss our numerical scheme for propagating the simulation forward in time.

VII. SUMMARY OF NUMERICAL SCHEME

Here, we describe the numerical method for evolving our system through time. We use explicit finite differencing in combination with numerical viscosity. The exact single-fluid RMHD equations (7) are marginally stable, which is to say, the Fourier components of the linearized equations have strictly real eigenvalues with no growth or decay. However, these equations become unstable when discretized in a numerical scheme. Numerical viscosity is needed in order to restore stability to the system. This includes momentum viscosity and magnetic resistivity. Our scheme has fourth-order accuracy in both space and time, and uses a rapidly convergent algorithm developed by Newman [26] to recover the primitive variables from conserved quantities.

We begin by physically motivating the RMHD single-fluid conservative equations (7). Within a given volume of fluid, the total rate of change of a given conserved quantity is equal to the flux of that quantity through the boundaries of that volume. Let C_i be the density of a given conserved quantity, and F_{ij} the flux density of that quantity in the direction $\hat{\mathbf{e}}_j$. Let $d\tau$ denote a volume element of the volume under consideration (i.e., the volume over which we integrate C_i), and let da_j denote the jth component of the area vector normal to a given location on the surface bounding this volume. Then, mathematically, we have

$$\frac{\partial}{\partial t}\int C_i d\tau + \oint F_{ij} da_j = 0. \tag{14}$$

With the use of the divergence theorem, we can rewrite (14) as follows:

$$\frac{\partial}{\partial t}\int C_i d\tau + \int \frac{\partial F_{ij}}{\partial x_j} d\tau = 0. \tag{15}$$

When we remove the volume integrals, the RMHD conservation equations take the general form

$$\frac{\partial C_i}{\partial t} + \frac{\partial F_{ij}}{\partial x_j} = 0, \tag{16}$$

where the x_j refer to the x, y, and z directions of a Cartesian coordinate system. This is the form of the single-fluid RMHD equations used in Anile [51]. The C_j are the conserved quantities. The F_{ij} are the corresponding flux quantities. The C_j and F_{ij} are given by Eqs. (8) in Sec. IV. The C_j are also listed explicitly in Eq. (A2) of Appendix A. If there is no net flux through the boundaries of a given volume of fluid, then the corresponding conserved quantity is conserved within that volume. This is true of the boundaries of our numerical system, which is a slab in the x-z plane. It therefore follows that throughout our simulations, the total conserved quantities (integrated over the numerical system) are in fact conserved. These are the C_j.

When we incorporate viscosity, the RMHD conservation-diffusion equations take the general form

$$\frac{\partial C_i}{\partial t} + \frac{\partial F_{ij}}{\partial x_j} = \eta_i \frac{\partial^2 C_i}{\partial x_j^2}. \tag{17}$$

The term on the right represents numerical viscosity, which, although it redistributes energy within the system, is formally conservative. Numerical viscosity is included for purposes of numerical stability. The exact RMHD single-fluid equations are marginally stable, i.e., the Fourier components of the linearized equations have strictly real eigenvalues and therefore display no growth or damping. However, when we discretize the spatial and temporal derivatives in a numerical scheme, these equations become unstable. We therefore need to include diffusion in order to restore stability to the system. Because diffusion is second order in space, the use of fourth-order spatial and temporal methods gives us explicit control over the viscosity coefficients. Diffusion in relativistic systems can produce certain anomalies associated with frame transformations. However, these do not emerge in our numerical simulations, as we remain in the stationary frame established by the velocity shear. The viscosity coefficients are chosen to be large enough to restore stability to the system, while still small enough for the nonlinear evolution to be approximately convergent with respect to viscosity. The viscosity coefficients correspond to Reynolds numbers of about 5000, which are most likely one or more orders of magnitude smaller than the Reynolds numbers of relevant astrophysical environments [60,61].

At each time step of a simulation, we evolve the system in several steps. We first use the numerical relaxation scheme of Newman [26], described in Appendix B, to recover the primitive variables (density, pressure, velocity, magnetic field) from the conserved quantities. We then use the fourth-order method of lines [62] to compute the spatial derivative of the flux quantities. We finally use the fourth-order Runge-Kutta method [58] to compute the conserved quantities at the next time step. These methods are discussed in more detail in the Appendixes.

We have described the numerical methods for initializing the system and for evolving the simulation in time. We now examine the results of these simulations for a set of representative field strengths.

VIII. RESULTS

In this section, we examine the evolution of the system after being perturbed by a KH-unstable mode. In Sec. VIII A, we describe the parameters of the simulations being examined. We then consider the unmagnetized case, in Sec. VIII B, in which we observe the formation of large counter-rotating vortices which persist well into the nonlinear regime. We then introduce a magnetic field, in Secs. VIII C through VIII F, and observe that the KH-unstable vortices are inhibited through a series of stages, namely, field amplification, vortex disruption, turbulent breakdown, and relaxation to an equilibrium state in which the flow and field are longitudinally aligned. Qualitatively similar stages are described in MHD literature. Here, we examine in detail how and to what extent these stages manifest in RMHD for a set of representative field strengths. Recall that in Sec. VI B, we defined a relativistic extension of the Alfvénic Mach number which we denoted M_A, and which is given by Eq. (13). We observed that the fractional reduction in linear growth rate is closely correlated with M_A. So, too, is the influence of a magnetic field on the nonlinear evolution of the KH instability. We demonstrate this in Sec. VIII I by comparing results for two different unperturbed flow speeds, and finding close agreement. We consider initial field strengths corresponding to $M_A = 41.4$, 20.7, 10.3, and 5.1, each successive value being half of the former.

We observe that for weaker fields, there is more vortex development, more magnetic reconnection, and more turbulent reorganization, causing the jet to broaden considerably. Vortex disruption corresponds to a disruption of the faster-moving components of the flow as mechanical energy is dissipated, leaving a slower-moving background flow. Stronger fields suppress these processes, resulting in less jet broadening. Sufficiently strong fields ($M_A = 5.1$) suppress vortex formation altogether, resulting in an immediate transition to an equilibrium state. In Sec. VIII G, we discuss several bifurcations, i.e., energy-transfer processes which are optimized for intermediate field strengths. Namely, viscous dissipation is optimized for intermediate vortex-disruptive fields. On the other hand, electromagnetic energy is maximized for the strongest fields which still allow partial vortex formation. In Sec. VIII H, we examine the time evolution of the flow more closely. For representative initial field strengths, we first study the evolution of a cross section of the longitudinal velocity, and then the time dependence of the spatially averaged Alfvénic Mach number. In Sec. VIII K, we compare our results with observations of astrophysical jets, and identify a possible explanation for observations of the knots in the radio jet M87. In Sec. VIII J, we determine the numerical accuracy with which our results satisfy a condition of alternating symmetry in the vorticity, which results from the symmetry of the unperturbed velocity profile and antisymmetry of the pressure perturbation profiles.

Throughout this section, we examine displays of two quantities, namely, the vorticity (curl of the velocity, directed along the y axis) and the longitudinal velocity, where the flow direction (z direction) is upward. To the immediate right of each display is a color scale indicating the correspondence between colors and numerical values, where dark blue (the coloration at the bottom of the scale) corresponds to the

minimum value and dark red (the coloration at the top of the scale) corresponds to the maximum value. The vorticity highlights the spatial contrast between the emergent nonlinear features. However, what one actually observes are the velocity components, density, etc. In the magnetized cases, the vorticity and longitudinal velocity decrease substantially through the nonlinear regime, and it should be noted that the color scales are adjusted accordingly in order to preserve the spatial contrast of the features being displayed. When the vorticity displays are viewed in black and white, darkly shaded areas correspond to high vorticity, and lightly shaded areas to low vorticity. When the longitudinal velocity displays are viewed in black and white, darkly shaded regions in the central flow correspond to high flow speed, while the darkly shaded ambient background corresponds to a negligible flow speed.

We begin, in the first subsection, by describing the simulation parameters of the various cases being studied.

A. Simulation parameters

In each case examined, we assume uniform unperturbed pressure P_0, density ρ_0, and magnetic field B_0, where the magnetic field is aligned with the flow. In particular, we have $P_0/(\rho_0 c^2) = 50$. The unperturbed velocity is moderately relativistic, with a shear variation given by

$$v_{z0}(x) = 0.7\, c\, \mathrm{sech}^2(x/r_0). \tag{18}$$

We assume an adiabatic index of $\Gamma = \frac{4}{3}$, consistent with a relativistic photon gas. The unperturbed sound speed is

$$c_s = c\sqrt{\frac{\Gamma P_0}{w_0}} = c\sqrt{\frac{\Gamma P_0}{\rho_0 c^2 + \Gamma P_0/(\Gamma - 1)}} = 0.576\, c. \tag{19}$$

This is close to the maximum physically allowable adiabatic sound speed of $c/\sqrt{3}$, and therefore corresponds to a pressure-dominated, relativistically hot, fluid. The perturbation has a longitudinal wave number $k_z = 0.8/r_0$, which is roughly the value corresponding to maximum growth. The time increment is $\Delta t = 0.032\, r_0/c$. The grid spans 1001 points in the x direction and 201 points per wavelength in the z direction. The spatial extent of the system is as follows:

$$-15.75\, r_0 \leqslant x \leqslant 15.75\, r_0, \tag{20}$$

$$0 \leqslant z \leqslant 4\pi/0.8\, r_0 \quad \text{(two wavelengths)}, \tag{21}$$

so that the spatial increments are $\Delta x = 0.0315\, r_0$ and $\Delta z = 0.0393\, r_0$.

We have verified that our results are convergent with respect to time step, and approximately convergent with respect to spatial increment [63]. The system spans two perturbation wavelengths in the longitudinal direction. However, we have found that the results are approximately independent of the number of longitudinal wavelengths spanned by the system, which is to say, the flow retains the spatial periodicity of a single perturbation wavelength [63]. Therefore, throughout this section, the displays show only one wavelength of the system. Transverse acoustic waves are present in the nonlinear regime, and their back-and-forth propagation is influenced by the system width. However, by comparing results for two different system widths, we have verified that the evolution of the flow, and its interaction with the magnetic field, are approximately independent of system width [63].

TABLE I. Linear parameters of representative cases. Time is in units of r_0/c.

$(M_A, \beta, v_A/c)$	$\omega_i r_0/c$	$T_i = 1/\omega_i$	$T = 2\pi/\omega_r$
Unmagnetized	0.0994	10.06	22.61
(82.8,3550,0.012)	0.0993	10.07	22.61
(41.4,888,0.024)	0.0990	10.10	22.63
(20.7,222,0.047)	0.0980	10.20	22.68
(10.3,55.5,0.095)	0.0943	10.67	22.89
(5.15,13.9,0.189)	0.0738	13.55	23.70

The exact RMHD single-fluid equations in (7) are marginally stable, but become unstable when discretized in a numerical scheme. Numerical viscosity is included in order to restore numerical stability to the system. The density and momentum viscosities (η_ρ, η_x, and η_z) are each $0.0002\, r_0 c$, while the viscosities in magnetic field components (η_{bx} and η_{bz}) are $0.0012\, r_0 c$. The numerical viscosities correspond to a Reynolds number of about 5000, which are most likely one or more orders of magnitude smaller than the Reynolds numbers of typical astrophysical environments [60,61]. Density viscosity is included in order to compensate for unphysical regions of negative density which emerge in the absence of mass transfer. We have verified that our simulation results are convergent with respect to viscosity, further detail of which is provided in Hamlin [63].

In Table I, we present the growth rate ω_i, growth time $T_i = 1/\omega_i$, and period $T = 2\pi/\omega_r$ for each of the cases studied. These emerge from the linear analysis performed in Sec. V. Corresponding to a given unperturbed field strength, M_A is the unperturbed relativistic Alfvénic Mach number, given by Eq. (13), $v_A = B_{z0}/\sqrt{w_0}$ is the unperturbed relativistic Alfvén speed, and $\beta = 2P_0/B_{z0}^2$ is the unperturbed plasma β. The large unperturbed plasma β values are characteristic of a pressure-dominated system, for which a given value of M_A corresponds to a smaller magnetic pressure than would be the case for a density-dominated system. However, when the magnetic field is amplified during the early nonlinear regime, the minimum plasma β is often of order unity. We have verified that for each magnetic field studied, the field remains divergenceless throughout the simulation [63]. We have also verified convergence of our results between the RHD, MHD, and RMHD regimes [63]. Further detail of these verifications is provided in Hamlin [63].

Having described the parameters of the cases being studied, we begin in the next section by examining the evolution of a relativistic KH-unstable flow in the absence of a magnetic field.

B. Evolution in RHD

We first consider evolution in the absence of a magnetic field, which also describes the early stages of evolution in many of the magnetized cases. At the start of the simulation, the system is perturbed in a KH-unstable numerical eigenmode as described in Sec. V. The system then evolves through a linear regime in which the perturbations grow. Deviations

from ideal growth are due to evanescent modes introduced by diffusion. After about eight growth times, the perturbations are comparable to the values of the unperturbed quantities, and energy is diverted from the linear mode into newly emergent nonlinear modes. This corresponds to a transition to the nonlinear regime, shortly after which the perturbed quantities saturate, at about 10 growth times. At this time, mechanical stresses have transverse components which have become comparable to the longitudinal components, causing the flow to twist, and resulting in the formation of two counter-rotating vortices on opposite sides of the flow axis, and separated by half the longitudinal perturbation wavelength. Note that throughout this Sec. VIII B, all displays of a given quantity use the same scale, where we use one scale for the displays of the vorticity (the curl of the velocity), and another scale for the displays of the longitudinal velocity.

The half-wavelength separation of the vortices is a direct consequence of the use of a linear mode with antisymmetric pressure perturbation profiles (a "sinuous" mode; see the end of Sec. V). If we instead used a mode with symmetric pressure profiles (a "varicose" mode), we would have pairs of adjacent vortices on either side of the flow axis. However, in a slab geometry, the sinuous mode grows much more quickly, which is why we use it. The resulting vortex formation is shown in the vorticity displays in Figs. 6(a) and 7(a). The vortices form around existing regions of low density and pressure associated with the distributions of the density and pressure perturbations. The y axis points into the page. Therefore, in the vorticity displays, blue coloration (negative vorticity) corresponds to counterclockwise fluid circulation, seen in the vortex in the region of negative x, i.e., the left half of the displays. Red coloration (positive vorticity) corresponds to clockwise fluid circulation, seen in the vortex in the region of positive x, i.e., the right half of the displays. The vortices themselves rotate in the direction of fluid circulation within them. As shown in Figs. 6(b) and 7(b), the center of the flow moves more rapidly, and therefore experiences larger mechanical stresses, causing it to twist by a larger amount than the slower-moving background flow.

We now consider nonlinear evolution, which occurs only in the absence of a magnetic field. The vortices are connected by dual filaments. Initially, vortex rotation is dominated by mechanical stresses, and the vortex shape and angular speed are both irregular, with the vortices alternately being elongated in the longitudinal and transverse directions, as seen by comparing Figs. 7 through 9. As time progresses, mechanical energy is viscously dissipated into thermal energy, and thermal stresses become larger in comparison to mechanical stresses. This is shown in Fig. 10. Because thermal stresses are isotropic,

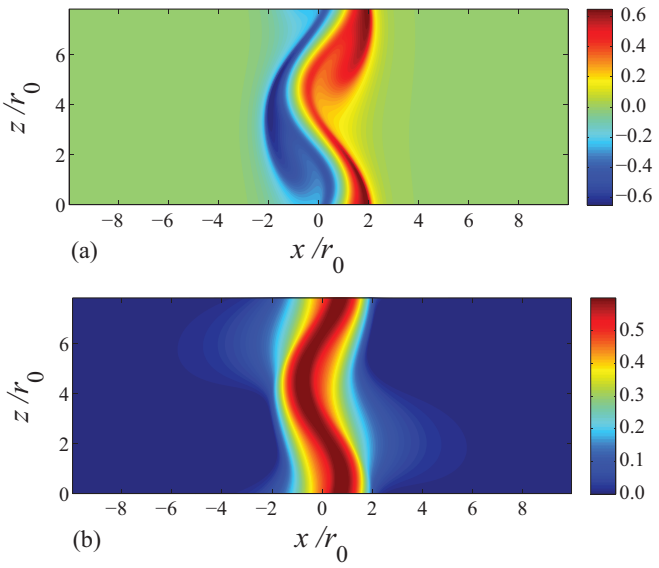

FIG. 6. (Color online) Unmagnetized evolution: (a) vorticity and (b) longitudinal velocity at $t = 7.33\,T_i = 3.26\,T = 73.7\,r_0/c = 1.35\,L_x/c_s$.

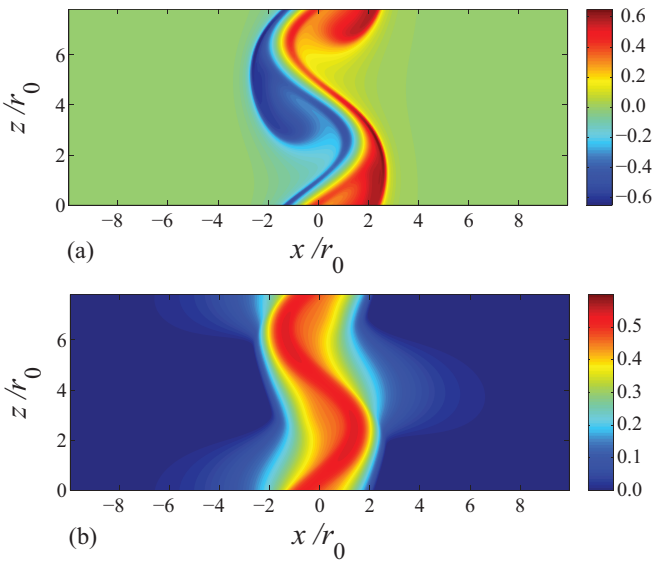

FIG. 7. (Color online) Unmagnetized evolution: (a) vorticity and (b) longitudinal velocity at $t = 7.94\,T_i = 3.53\,T = 79.9\,r_0/c = 1.46\,L_x/c_s$.

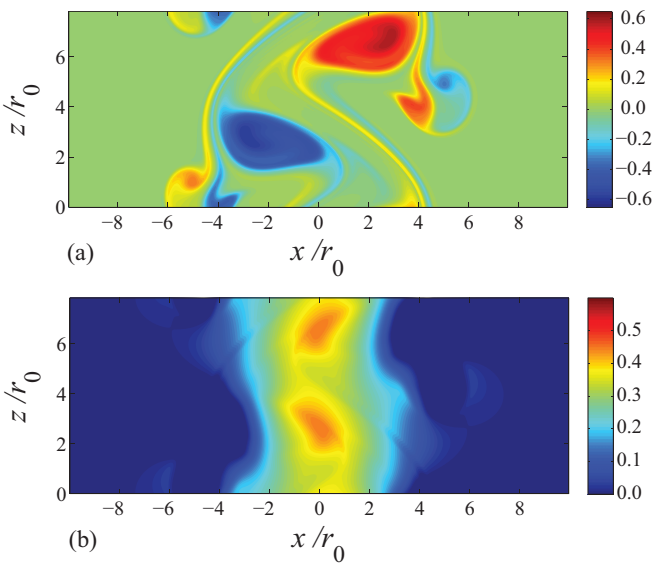

FIG. 8. (Color online) Unmagnetized evolution: (a) vorticity and (b) longitudinal velocity at $t = 14.04\,T_i = 6.25\,T = 141.3\,r_0/c = 2.58\,L_x/c_s$.

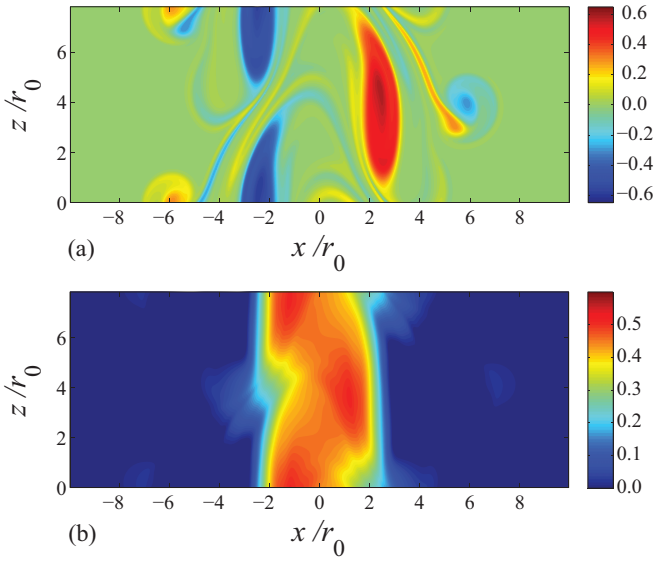

FIG. 9. (Color online) Unmagnetized evolution: (a) vorticity and (b) longitudinal velocity at $t = 16.49\,T_i = 7.34\,T = 165.9\,r_0/c = 3.03\,L_x/c_s$.

the vortices relax to a more regular ellipsoidal shape and a roughly constant angular velocity. They also relax to a more constant longitudinal pattern speed, which, due to viscous dissipation, has slowed to roughly 60% of the linear phase velocity.

On either side of the flow axis, we notice the formation of a pair of smaller adjacent secondary counter-rotating vortices at the outer transverse boundaries of the flow. The vortices circulate in opposite directions because they emerge from adjacent filaments of opposite vorticity (specifically, these are the filaments that initially connected the primary vortices). These smaller vortices also do not propagate downstream. Downstream propagation is correlated with the linear phase velocity, and in the linear regime the pattern speed is equal to the linear phase velocity. The large primary vortices emerge from linear features of the flow (alternating regions of low density and pressure), and their downstream propagation is a result of the linear pattern speed of these features. However, the smaller secondary vortices emerge from nonlinear features which are not present in the linear evolution, and therefore do not propagate downstream with the flow.

We have examined the nonlinear evolution of a relativistic flow in the absence of a magnetic field, and found that the KH-unstable vortices persist. We now examine the manner in which these vortices are inhibited in the presence of a magnetic field. We begin, in the next section, with a fairly weak vortex-disruptive field for which $M_A = 41.4$.

C. Weak vortex-disruptive field ($M_A = 41.4$)

We now introduce a magnetic field which is not strong enough to suppress vortex formation but is strong enough to disrupt and inhibit nonlinear vortices after they have formed. This field corresponds to $M_A = 41.4$ (see Table I for relevant parameters).

Figures 11 through 13 each show displays of the vorticity, at a given time in the simulation, for the (a) unmagnetized case considered in the previous section, and (b) magnetized case described above. In the magnetized case, the display is overlaid with contours of the magnetic field lines, which demonstrates the close complementarity between flow and magnetic field behavior. The unmagnetized and magnetized displays have slightly different sizes, due to the fact that the unmagnetized displays span a larger transverse width of the system. An important feature of the magnetized evolution, that should be noted in the displays in this section and other sections discussing magnetized evolution, is the remarkable complementarity between the fluid behavior and the behavior of the magnetic field. This can be seen in the close correspondence between the field lines and various flow-related

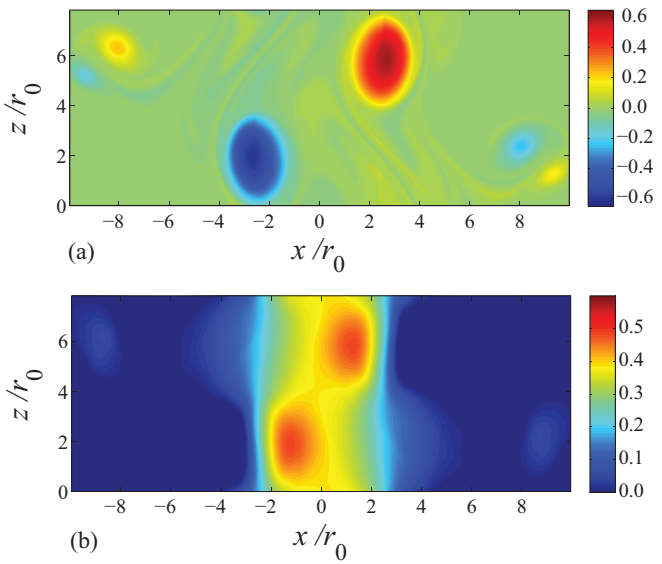

FIG. 10. (Color online) Unmagnetized evolution: (a) vorticity and (b) longitudinal velocity at $t = 32.97\,T_i = 14.67\,T = 331.8\,r_0/c = 6.07\,L_x/c_s$.

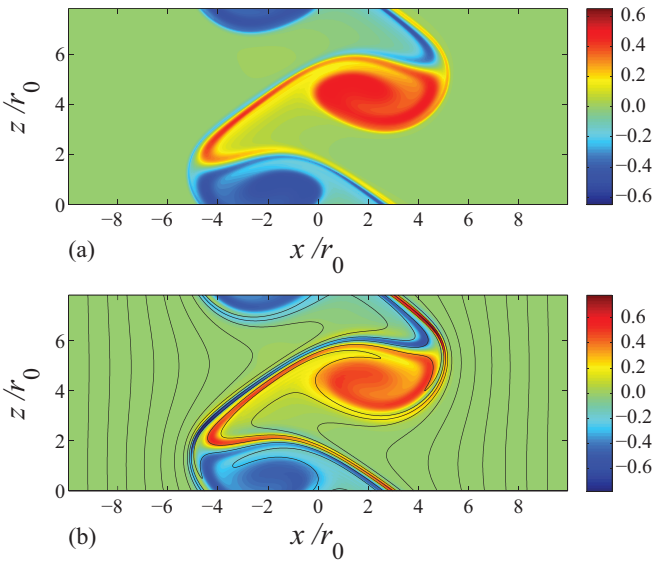

FIG. 11. (Color online) Vorticity for (a) $B = 0$ and (b) $M_A = 41.41$ at $t = 9.8\,T_i = 4.3\,T = 98.3\,r_0/c$.

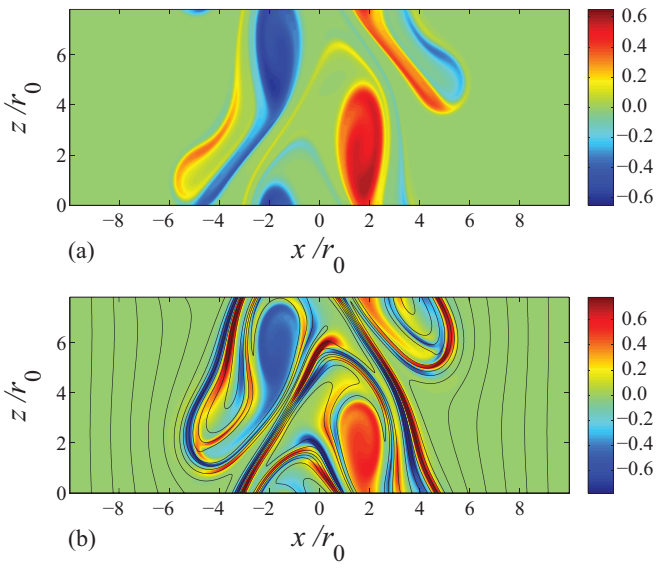

FIG. 12. (Color online) Vorticity for (a) $B = 0$ and (b) $M_A = 41.41$ at $t = 12.2\,T_i = 5.4\,T = 123\,r_0/c$.

quantities (vorticity, flow velocity, etc.), shown in the displays onto which the field lines are overlaid. Physically, the fluid is driving the field via thermal and mechanical stresses, and in turn, the tension in the field lines is constraining the fluid via electromagnetic stresses.

The evolution in the early nonlinear regime is almost identical to the evolution for the RHD case, as shown in Fig. 11. For $M_A = 41.4$, the case shown, this close agreement persists through 10 or 11 growth times, i.e., until just after the saturation stage. This period of agreement corresponds to the field amplification stage of vortex inhibition, during which the counter-rotating vortices expel plasma and magnetic field lines, resulting in low density and pressure in the vortices, and field amplification at the vortex extremities, along the filaments connecting the vortices. As the vortices rotate, they twist the

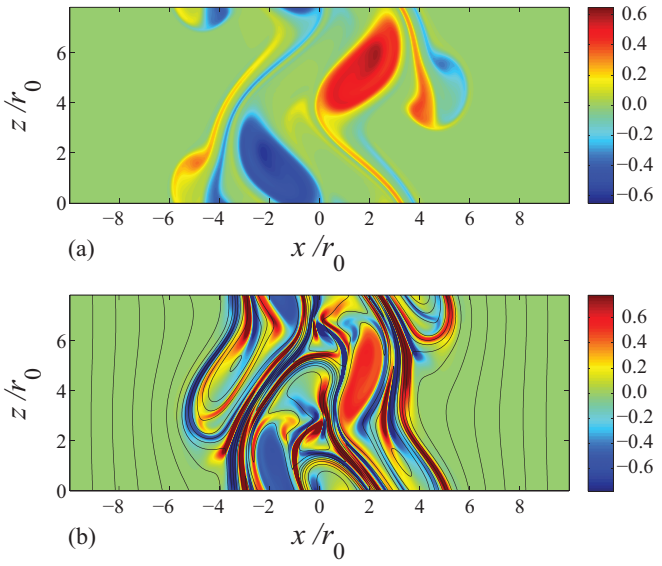

FIG. 13. (Color online) Vorticity for (a) $B = 0$ and (b) $M_A = 41.41$ at $t = 13.4\,T_i = 6.0\,T = 135\,r_0/c$.

field lines, which will lead to magnetic reconnection. In their studies of the extragalactic radio jet M87, Hines *et al.* [64] observed that while the field is generally aligned with the jet flow, there are large knots in which the field has a transverse component. Stawarz *et al.* [65] deduced that the magnetic field inside knot A of M87 has an amplified value of at least 300 μG, where the field elsewhere is less than about 100 μG [64]. These observations are consistent with the knots of M87 exhibiting vortexlike behavior, twisting the field lines into configurations with transverse components, and centrifugally expelling them to vortex extremities, thereby amplifying them. We will discuss this further in Sec. VIII K.

This amplification results in vortex shedding of amplified hybrid filamentary features, which signals the start of the next stage of vortex inhibition, i.e., vortex disruption, where we begin to see deviations between the magnetized and unmagnetized cases. In Fig. 12, at 12.2 growth times, the magnetized case contains enhanced filamentary features, and hybridization, not seen in the unmagnetized case. In Fig. 13, at 13.4 growth times, we see greater deviation between the two cases. The vortex disruption has progressed, and there is a greater population of features of enhanced vorticity. Also, the unmagnetized vortices have undergone more rotation than the magnetized vortices. The amplified magnetic field therefore exerts stresses that substantially decelerate the overall vortex rotation. At the same time, these stresses result in vortex deformation. Again, from examining Fig. 13, the magnetic field also suppresses the formation of the pairs of secondary vortices seen in the unmagnetized case. In their place, we instead see magnetic reconnection occurring in pocketlike regions on either side of the flow. Filamentary features, as described above, have been observed in numerous jets, including the cosmic double helix in 3C 273 [19], the ribbons and threads in 3C 120 [17,18], and the filaments in the radio lobes of M87 [64]. These filaments may be the result of field-induced vortex shedding during the disruptive stage, or may possibly be similar to the dual filaments connecting the vortices throughout vortex evolution, i.e., the filaments along which the field is amplified, as discussed in Sec. VIII K.

After vortex disruption, the next stage of inhibition is turbulent breakdown into smaller-scale structures, which corresponds to further broadening and deceleration of the jet as electromagnetic and mechanical energy are viscously dissipated into thermal energy. The jet then relaxes to an equilibrium configuration consisting of flow-aligned vortex and current filaments. We will discuss these stages in more detail in what follows. We should mention that the small-scale features in the turbulent regime are influenced to some extent by reverberations of acoustic waves from the transverse boundaries of the system. However, the vortex-disruptive phase (up to about 16 growth times) is independent of system width, and in the turbulent and equilibrium phases, the system width does not significantly influence the evolution of the flow or the magnetic field.

In Fig. 14, at 11.6 growth times, the vortices have expelled the field lines, resulting in amplified field, along with amplified alternating current layers, at the vortex extremities, and along the filaments connecting the vortices. There is almost no current in the vortex interiors, but the current diffuses into the regions into which the field lines are being twisted by

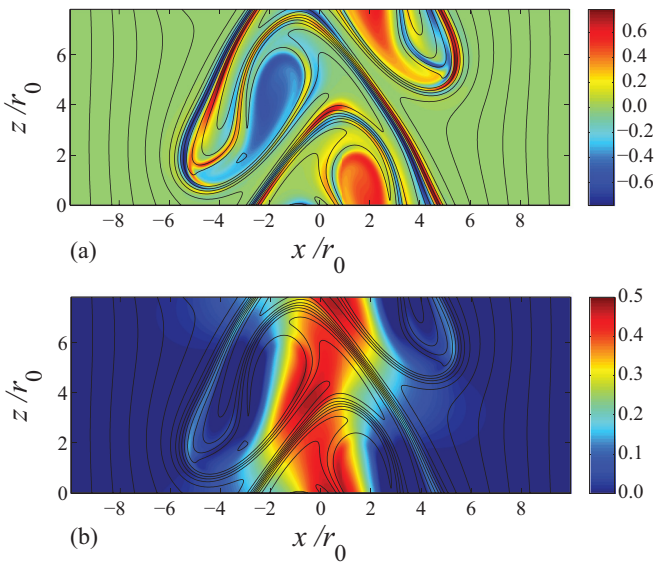

FIG. 14. (Color online) (a) Vorticity and (b) longitudinal velocity at $t = 11.6\,T_i = 5.16\,T = 117\,r_0/c$, where $M_A = 41.4$, $\beta_{\min} = 2.09$.

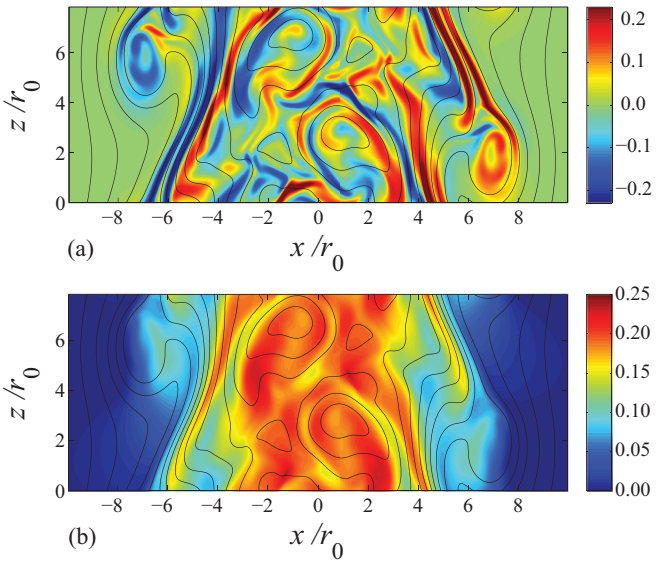

FIG. 16. (Color online) (a) Vorticity and (b) longitudinal velocity at $t = 27.4\,T_i = 12.2\,T = 276\,r_0/c$, where $M_A = 41.4$, $\beta_{\min} = 27.2$.

vortex rotation, i.e., the regions where magnetic reconnection will take place. Vortex rotation is closely correlated with the deformation of the flow, as seen in Fig. 14(b). This is the approximate time when the vorticity, current density, and electromagnetic energy reach their maximum values. The minimum plasma β at this time is 2.09, which is close to the smallest value that occurs for this simulation, and is less than $1/400$ of the unperturbed plasma β. There is minimal vortex disruption by the field, and therefore the evolution of the flow, until this point, very closely resembles the evolution for the corresponding unmagnetized case. Although the central flow has not widened noticeably, the region of nonzero vorticity has widened to almost three times the initial jet width, indicating a broadening of the outer slower-moving regions.

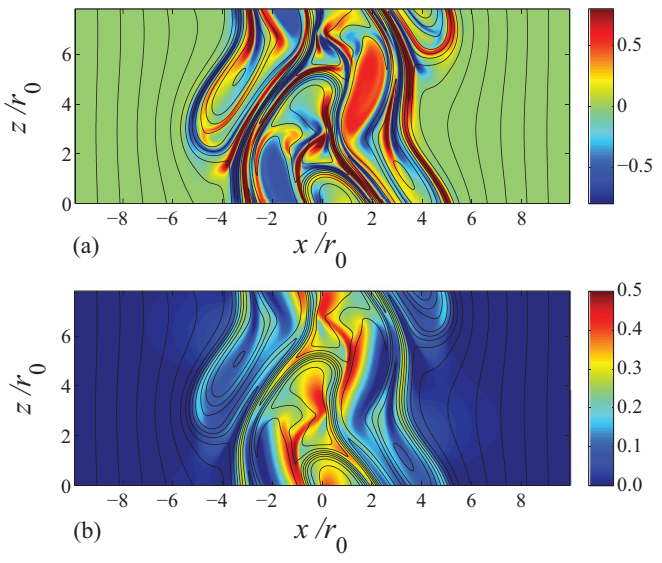

FIG. 15. (Color online) (a) Vorticity and (b) longitudinal velocity at $t = 13.4\,T_i = 5.97\,T = 135\,r_0/c$, where $M_A = 41.4$, $\beta_{\min} = 3.38$.

In Fig. 15, at 13.4 growth times, magnetic stresses at the vortex boundaries have resulted in significant vortex disruption. This disruption takes the form of significant vortex shedding of amplified hybrid filamentary features (seen in the vorticity display), and deformation of the vortex shape. By examining the previous comparison, in Fig. 13, of the vorticity display with the corresponding unmagnetized case, we can isolate the vortex deformation which is due specifically to magnetic stresses, as opposed to mechanical and thermal stresses. Specifically, magnetic stresses have not yet caused significant deformation, but are gradually making the vortices narrower, more elongated, and more irregular in shape. As shown in Fig. 15(a), the hybrid filamentary features take the form of thin layers at the vortex boundaries, and a complex structure that emerges between the vortices. Magnetic stresses also cause rapid angular deceleration, halting vortex rotation at the orientations shown in the vorticity display. Magnetic reconnection has occurred in the pocketed regions into which the vortices have twisted the field lines (i.e., the regions into which the current has diffused). The field, and current layers, are still amplified along the interconnecting filaments. From the display of longitudinal velocity, the vortex disruption closely complements the disruption of the faster-moving components of the flow, due to magnetic stresses exerted by amplified field lines. The jet has widened to about three times its initial width, and has decelerated to about $0.4\,c$.

In Fig. 16, at 27.4 growth times, the vortices are no longer visible, and the system is well into the turbulent regime. Note that, in order to preserve spatial contrast, the color scales each span a smaller range. The boundaries of many features have been smeared by viscous dissipation. Two factors are likely involved in the enhancement of viscous dissipation. Turbulent breakdown results in structures whose length scales are more comparable to the length scales associated with diffusion. Also, the average vorticity has decreased by a factor of almost 4, which is more comparable to the frequencies of modes introduced by diffusion. The system therefore has a higher

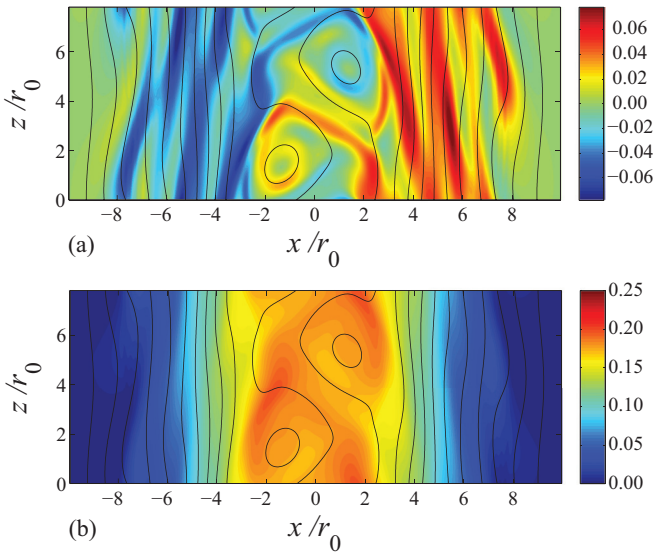

FIG. 17. (Color online) (a) Vorticity and (b) longitudinal velocity at $t = 56.6\,T_i = 25.3\,T = 571\,r_0/c$, where $M_A = 41.4$, $\beta_{\min} = 182$.

correlation with viscous processes, enabling a greater amount of energy transfer via viscous interactions. The field and current have lost much of their amplification, however, there are numerous areas of magnetic reconnection in the central region. Two large central reconnected regions appear to drive persistent vortical behavior. Filaments of enhanced vorticity are concentrating in layers on the left and right boundaries of the flow. A downstream-aligned central flow, of about $7.0\,r_0$ in width, i.e., twice the initial jet width, is in the process of forming, and over time, is becoming more spatially uniform. This process began as soon as the vortices were inhibited, and the magnetic field began to lose its amplification. The flow has continued to decelerate, due to viscous dissipation, and now has a maximum flow speed of about $0.25\,c$. The central flow is still somewhat heterogeneous, and contains components with flow speeds ranging from about $0.15\,c$ to about $0.25\,c$. The regions of minimum flow speed tend to be located between vortex filaments of opposite vorticity. The central flow region is a region of low density, from which plasma has been expelled.

In Fig. 17, at 56.6 growth times, the system is now approaching an equilibrium state consisting of flow-aligned vortex and current filaments. Note that, in order to preserve spatial contrast, the color scales each span a smaller range. The width of these filaments is, on average, about $0.9\,r_0$ (i.e., $\frac{1}{4}$ the initial jet width). The filaments are somewhat smeared due to diffusion, partly for the reasons mentioned in the previous paragraph (i.e., the vorticity is now only about $\frac{1}{8}$ of its initial value, and is therefore more closely tuned to the frequencies of modes associated with diffusion). The filaments surround a central region of persistent vortical behavior, driven by magnetic reconnection, although both the field lines and vortical filaments are gradually becoming aligned with the flow. These reconnected regions correspond to locally amplified current density. We can now see that this coincides with the low-density central flow region. Meanwhile, the jet has widened to roughly 4.5 times its initial width. The jet has continued to decelerate, and the central flow region has become more homogeneous, so that the central flow speeds range from roughly $0.15\,c$ to $0.2\,c$. While the current filaments alternate spatially, the vortex filaments have more spatial uniformity, with filaments of positive vorticity to the right of the flow, and filaments of negative vorticity to the left of the flow. The flow is maximized in the central region, and vanishes asymptotically at the transverse boundaries. This indicates that, despite the complex intermediate reorganization brought on by magnetic and mechanical stresses, the flow has retained a qualitative memory of its initial configuration. Similar results were also seen in the MHD studies of Ryu *et al*. [28] and Frank *et al*. [27].

In the next section, we examine an unperturbed magnetic field which is twice as strong as the one just examined. We will find that the inhibition processes described above occur more rapidly.

D. Intermediate vortex-disruptive field ($M_A = 20.7$)

We have examined the stages of vortex inhibition for a fairly weak vortex-disruptive field for which $M_A = 41.4$. We now examine how this process is modified for stronger fields. In general, any field in the vortex-disruptive regime (M_A larger than about 6) inhibits vortex development through the processes described above (field amplification, vortex disruption, turbulent breakdown into smaller-scale structures, and relaxation to an equilibrium state consisting of flow-aligned vortex and current filaments). However, for stronger fields, these processes occur more rapidly (i.e., after a smaller number of growth times), and the jet does not widen by as large a factor. In the above case ($M_A = 41.4$), vortex disruption is not noticeable until 12 growth times, and even after 60 growth times, the system has not completely relaxed to its equilibrium state, due to the persistent vortical behavior in the central region.

Figures 18 through 20 show the stages of vortex inhibition for a field corresponding to $M_A = 20.7$ (see Table I for relevant parameters). Here, vortex disruption is noticeable after 10

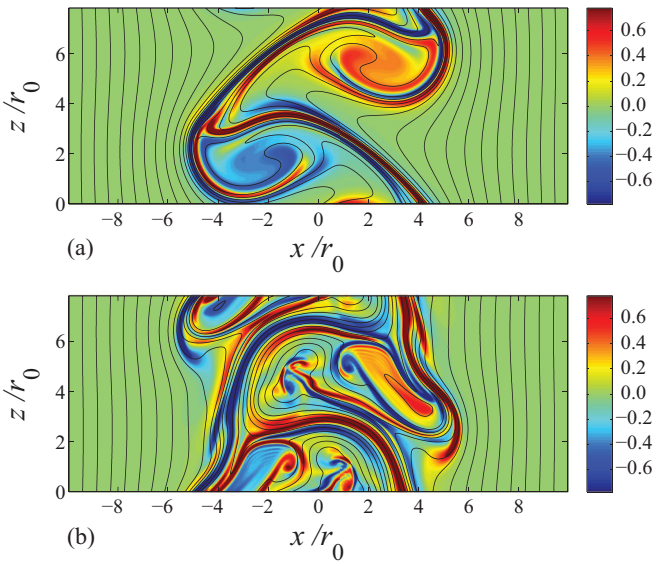

FIG. 18. (Color online) Vorticity for $M_A = 20.7$ at (a) $t = 10.2\,T_i = 4.61\,T = 104\,r_0/c$, $\beta_{\min} = 1.43$ and (b) $t = 13.9\,T_i = 6.23\,T = 141\,r_0/c$, $\beta_{\min} = 4.26$.

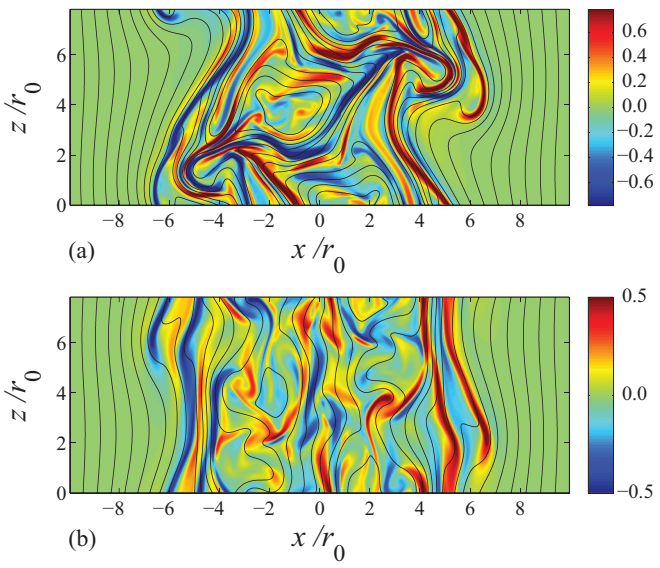

FIG. 19. (Color online) Vorticity for $M_A = 20.7$ at (a) $t = 16.3\,T_i = 7.31\,T = 166\,r_0/c$, $\beta_{\min} = 5.79$ and (b) $t = 23.5\,T_i = 10.6\,T = 240\,r_0/c$, $\beta_{\min} = 15.4$.

growth times [see Fig. 18(a)] versus about 13 growth times for $M_A = 41.4$, and the system has almost reached an equilibrium filamented state after 37 growth times (see Fig. 20), with an equilibrium jet width of about $15\,r_0$ (about four times the initial jet width). Recall that for $M_A = 41.4$, even after almost 60 growth times, the system still has not reached an equilibrium state. In the case for which $M_A = 20.7$, there is less magnetic reconnection, and vortices therefore do not persist in the central region. In particular, for $M_A = 20.7$, the vortices are inhibited at an earlier point in their rotation, before they can twist the field lines to the point where they reconnect in pocketlike regions along the sides of the flow [see Fig. 18(b)].

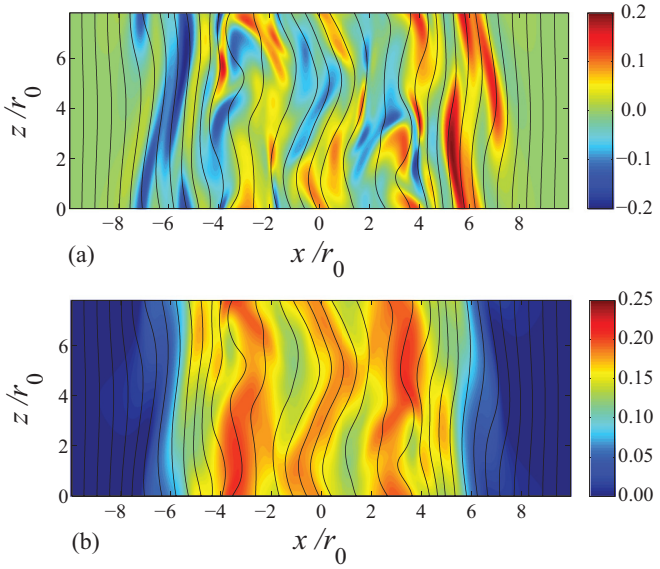

FIG. 20. (Color online) (a) Vorticity and (b) longitudinal velocity at $t = 37.9\,T_i = 17.1\,T = 387\,r_0/c$, where $M_A = 20.7$, $\beta_{\min} = 35.9$.

We now examine the displays for $M_A = 20.7$ in more detail. Figure 18(a), at 10.2 growth times, displays the vorticity when the electromagnetic energy is approaching its approximate maximum value. The primary vortices have formed (the large eddy structures), and as they rotate are expelling the field lines, which as a result are concentrated along the central filaments. Electromagnetic energy, electromagnetic momentum, current density, and vorticity are all maximized along the central filaments. The vortices are twisting the field lines as they rotate. Even though electromagnetic energy, current density, etc., have not yet reached their maximum values, magnetic stresses have already begun to disrupt the vortices, as seen by narrow filaments of the opposite vorticity which extend into each primary vortex. Through vortex twisting and diffusion, the field lines are beginning to infiltrate the regions between the vortices.

We now proceed to Fig. 18(b), which displays the vorticity at 13.9 growth times. The electromagnetic energy density and vorticity have previously reached their peak values, and are now decreasing, as seen by the fact that the field lines are less concentrated. Magnetic stresses have brought vortex rotation to a halt, so that they remain in the orientations shown. These stresses also deform the vortices into the irregular shapes shown, and result in the emergence of enhanced hybrid filamentary features. These include the narrow layers of opposite vorticity at the vortex boundaries, and the complex hybrid structure in the interior region between the vortices, which is formed by layers of filament which magnetic stresses have peeled from the primary filament and the base of the vortex. This latter structure is modulated by magnetic reconnection occurring among field lines which have infiltrated the interior, as a result of vortex twisting and field diffusion. Note that the vortices fail to twist the field lines to the point where they reconnect in pocketlike regions along the sides of the jet, as occurs for the weaker field $M_A = 41.4$. The vorticity and electromagnetic energy are still maximized in the primary filaments, which are still intact, although these have detached from the bases of the vortices. The jet has widened to about three times its initial width.

We now proceed to Fig. 19(a), which displays the vorticity at 16.3 growth times. The system has transitioned from the disruptive to the turbulent regime, as the primary vortices are no longer visible. Electromagnetic and mechanical energy are being viscously dissipated into thermal energy. Viscous dissipation has smeared the hybrid structures that emerged in the interior regions, so that these are much less sharply defined, though magnetic reconnection persists. The dissipation of these hybrid structures is due to their smaller length scales and smaller vorticity, which are more comparable, respectively, to the length scales and frequencies associated with diffusion. Vorticity and electromagnetic energy are still maximized along the primary filaments, which are narrower and have been expelled from the central region by mechanical stresses, and by magnetic stresses associated with reconnection. These filaments still retain much of the initial curvature that developed during formation of the primary vortices. The jet has now widened to about 3.4 times its initial width.

We now proceed to Fig. 19(b), which displays the vorticity at 23.5 growth times. Note that, in order to preserve spatial contrast, the color scales each span a smaller range. The

system is well into the turbulent regime. About $\frac{2}{3}$ of the peak electromagnetic energy has been viscously dissipated from the system, resulting in a loss of field line concentration, and a decrease in vorticity in the primary filaments, which have now been expelled to the left and right boundaries, and have lost their curvature and become aligned with the flow. The primary filaments have also shed fragments of enhanced vorticity which lie along the central axis, and are interspersed elsewhere in the interior. Throughout the interior are small turbulent structures, which have been viscously smeared due to the close correlation between the small length scales and vorticity of these structures, and the length scales and frequencies introduced by diffusion. The turbulent features are partly driven by persistent magnetic reconnection. The jet has now widened to about 3.6 times its initial width, and decelerated from a flow speed of $0.7\,c$ to about $0.3\,c$.

We now consider Figs. 20(a) and 20(b), which display the vorticity and longitudinal velocity, respectively, of the system at 37.9 growth times, as it approaches an equilibrium state consisting of flow-aligned filaments (note change in vorticity color scale, in order to preserve spatial contrast). The vorticity is maximized in the outer filaments, but has decreased to about a quarter of its peak value, and is therefore more closely tuned to frequencies of modes introduced by diffusion, resulting in widening of the filaments due to viscous smearing. The magnetic field lines are more closely aligned with the flow, as are the turbulent features, which are developing into vortex filaments. The jet has broadened to about four times its initial width (based on the vorticity display), while the central flow region is about three times the initial jet width, and is much broader and more heterogeneous than the equilibrium central flow for the weaker field $M_A = 41.4$. The central flow consists of several regions whose flow speed is about $0.2\,c$ interspersed with a background flow whose speed is about $0.12\,c$. In particular, there is a narrow strip, along the central axis, whose flow speed is about $0.18\,c$. For stronger fields, we will also observe narrow central strips of relatively high flow speed. However, these central channels will be surrounded by much slower uniform background flows. The central channel in a broad heterogeneous flow, as shown in Fig. 20(b), represents an intermediate configuration between the broad, more homogeneous equilibrium flow of a weak field, with no central channel, and the equilibrium flow of a strong field, which has a relatively fast central channel surrounded by a slower background flow. Recall that a weak field, such as $M_A = 41.4$, has more magnetic reconnection, resulting in vortical behavior that persists for many more growth times, than the present case ($M_A = 20.7$).

In the next section, we examine an unperturbed magnetic field which is twice as strong as the one just examined. This sheds light on the nature of vortex inhibition for a strongly vortex-disruptive field.

E. Strong vortex-disruptive field ($M_A = 10.3$)

We now consider the nonlinear evolution of a strong vortex-disruptive field for which $M_A = 10.34$ (see Table I for relevant parameters). Figures 21 through 23 show the stages of vortex inhibition. Here, vortex disruption is noticeable after 8.5 growth times, i.e., almost immediately after the vortices

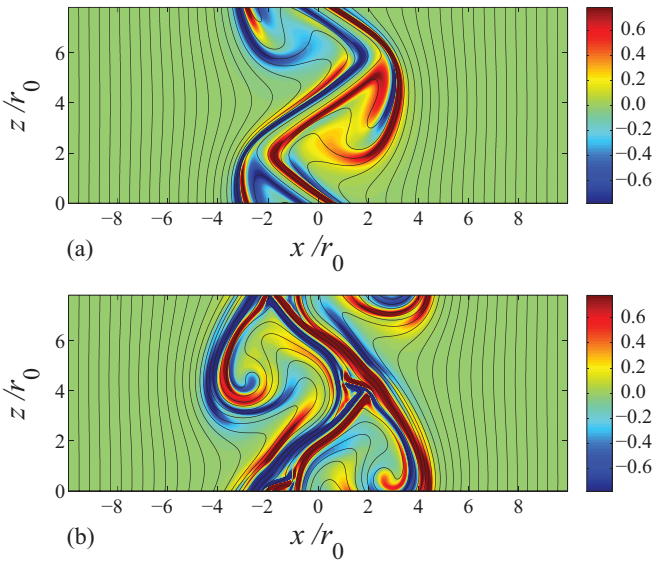

FIG. 21. (Color online) Vorticity for $M_A = 10.3$ at (a) $t = 8.64\,T_i = 4.03\,T = 92.2\,r_0/c$, $\beta_{\min} = 0.87$ and (b) $t = 10.9\,T_i = 5.10\,T = 117\,r_0/c$, $\beta_{\min} = 2.79$.

begin to form (see Fig. 21), and the system has reached an equilibrium filamented state after about 25 growth times (see Fig. 23). The field $M_A = 10.34$ also inhibits magnetic reconnection, which occurs to a minimal extent after about 12 growth times, as the field lines diffuse into the partially formed vortices [see Fig. 22(a)]. The equilibrium jet width is about $12\,r_0$, which is about 3.2 times the initial jet width. The equilibrium flow contains a narrow central region of high flow speed, low density, and width about $\frac{1}{5}$ the initial jet width, along with a background flow whose width is about 1.5 times the width of the initial flow [see Fig. 23(b)]. We will observe very similar equilibrium flow properties in Sec. VIII F, when we consider a field which is strong enough to suppress vortex

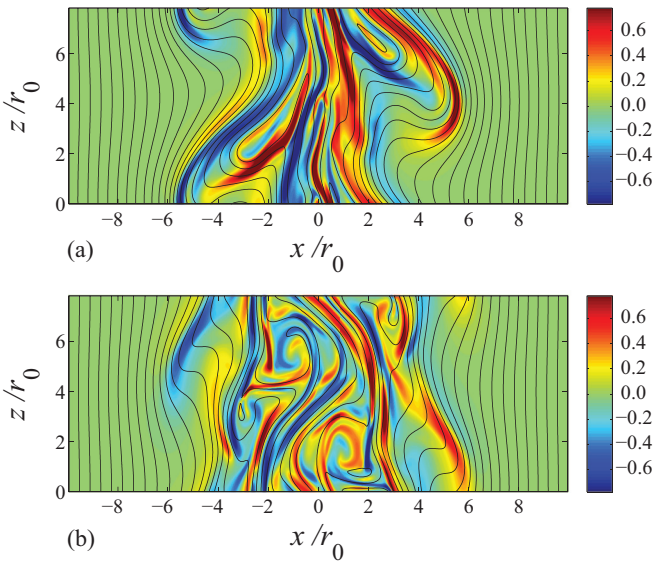

FIG. 22. (Color online) Vorticity for $M_A = 10.3$ at (a) $t = 13.2\,T_i = 6.17\,T = 141\,r_0/c$, $\beta_{\min} = 4.05$ and (b) $t = 16.7\,T_i = 7.78\,T = 178\,r_0/c$, $\beta_{\min} = 5.76$.

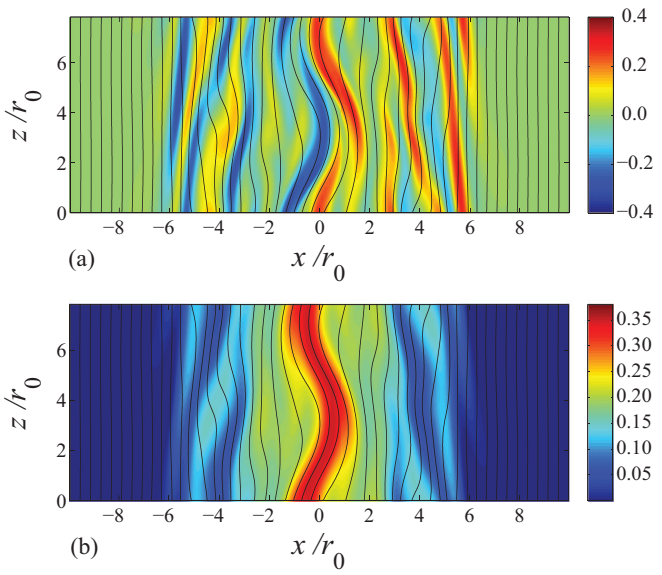

FIG. 23. (Color online) (a) Vorticity and (b) longitudinal velocity at $t = 27.1\,T_i = 12.6\,T = 289\,r_0/c$, where $M_A = 10.3$, $\beta_{\min} = 20.9$.

formation ($M_A = 5.145$). For this field, equilibrium is reached after about 20 growth times, and the jet only widens to about $8\,r_0$, which is about 2.25 times its initial width.

We now examine the displays for $M_A = 10.34$ in more detail. Figure 21(a), at 8.6 growth times, displays the vorticity at the approximate saturation stage in the early nonlinear regime. The partially formed vortices have already been disrupted by strong magnetic stresses. As these stresses oppose the rotation of the flow, it develops large shear variations where the magnetic tension is greatest, resulting in amplified filaments of high vorticity, and a large amount of electromagnetic energy being extracted directly from the bulk flow, energy that would otherwise be diverted into rotational form. The magnetic stresses also cause the interiors of the partially formed vortices to separate into regions of opposite vorticity, resulting in extensive hybridization before the vortices have the opportunity to acquire a well-defined clockwise or counterclockwise vorticity. The field lines have begun to diffuse into the partially formed vortices. We now proceed to Fig. 21(b), after 10.9 growth times. Maximum vorticity has been reached (after about 10 growth times), along with maximum electromagnetic energy. The filaments of maximum vorticity have thickened. The aforementioned regions of hybrid vorticity, which had permeated the vortical regions, are now compressed by magnetic tension into densely packed hybrid filament layers. The ends of these filaments curl sharply in response to the resistance exerted by magnetic stresses. This high curvature enhances the diffusion of magnetic field lines into the vortical regions, whose vorticity is almost entirely concentrated in the filaments at the boundaries. The jet has broadened to slightly over twice its initial width.

We now proceed to Fig. 22(a), after 13.2 growth times. The electromagnetic and mechanical energies are now being viscously dissipated into thermal energy. As a result, the vorticity has decreased considerably, and correspondingly, the central filaments have been viscously "smeared" into broader, more gradually sheared regions. As the magnetic stresses have decreased, the tips of the outer filaments have lost much of their previous curvature. A portion of densely packed filament became aligned with the central axis after about 12 growth times, and now this filament is separating into a thick hybrid structure in the central region. A small amount of magnetic reconnection is now visible in the vortical regions into which the field lines have diffused. Note that for a strong field such as this one, the movement of magnetic field lines is dominated not by vortex twisting, but by diffusion, which leads to much weaker reconnection, if any. The jet has broadened to almost three times its initial width. All of these processes signify the transition of the system into a turbulent regime. We now proceed to Fig. 22(b), after 16.7 growth times. The system is now well into the turbulent regime, and the vorticity has continued to decrease as more electromagnetic energy is viscously dissipated. The outer filaments have lost more of their curvature, and are becoming aligned with the flow, signifying the inhibition of the vortices that partially emerged in the early nonlinear regime. The central trunk, however, has spread into a larger central region of curved filaments surrounded by almost circular regions of newly emergent vortical behavior.

Finally, we proceed to Figs. 23(a) and 23(b), which display the vorticity and longitudinal velocity, respectively, after 27.1 growth times, as the system is approaching an equilibrium state consisting of flow-aligned filaments (note change in vorticity color scale, in order to preserve spatial contrast). The filament width is about $\frac{1}{5}$ the initial jet width, and the filaments are interspersed with viscously smeared regions of smaller vorticity of the opposite sign. These viscous regions formed at the boundaries of the jet in the early turbulent regime, as seen in Figs. 22(a) and 22(b). The jet has now broadened to about 3.2 times its initial width, which is its approximate equilibrium width. The flow consists of a narrow central strip of relatively high flow speed of about $0.4\,c$, and whose width is about $\frac{1}{4}$ the initial jet width. Surrounding this narrow flow are two vortex filaments, which show that this flow channel has relatively high shear at its boundaries. Also surrounding the flow channel is a background flow whose width is about 1.5 times the initial jet width, and whose flow speed has a nearly uniform value of about $0.2\,c$. This background flow coincides with the central vortical region described in Fig. 22(b). We will see that in the case of a vortex-suppressing field, the width of this background flow is nearly identical to the initial jet width.

We see that for stronger unperturbed fields, the vortices are inhibited at an earlier point in their rotation, and there is therefore less twisting of the field lines, which results in less magnetic reconnection. As the amount of reconnection diminishes, the reconnection that does occur is driven less by vortex twisting and to a greater extent by diffusion of the field lines. With less magnetic reconnection, the turbulent reorganization of the system is less complex, and the transition to a flow-aligned filamented state is more rapid. Apart from more rapid vortex inhibition, stronger fields also result in a suppression of both magnetic reconnection and of the complexity of turbulent breakdown. Correspondingly, for stronger unperturbed fields, the filament widths are narrower, and the equilibrium jet widths are narrower. Let W_0 denote the initial jet width and W_f the equilibrium jet width. For $M_A = 41.4$, $W_f \approx 4.5\,W_0$. For $M_A = 20.7$, $W_f \approx 4\,W_0$. For

$M_A = 10.3$, $W_f \approx 3.2\,W_0$. And for the vortex-suppressing field $M_A = 5.15$, $W_f \approx 2.25\,W_0$. These equilibrium widths correspond to an initial perturbation wavelength of $7.85\,r_0$. The equilibrium width seems to scale with input wavelength for weaker fields, but not for stronger fields. This may result from weaker fields that stimulate vortex rotation that has the effect of coupling longitudinal and transverse length scales.

We have examined fields that allow a certain amount of vortex formation. We now double the field strength once again, from $M_A = 10.3$ to 5.15, and examine a field that suppresses vortex formation entirely.

F. Vortex-suppressing field ($M_A = 5.15$)

We now consider a magnetic field which is strong enough to suppress vortex formation, which means that M_A is less than about 6. Specifically, $M_A = 5.15$. As before, the initial jet width is about $3.6\,r_0$. Figures 24 through 26 show the suppression of vortex formation, and the rapid transition to a flow-aligned filamented state. As before, each color display (vorticity and longitudinal velocity) is overlaid with contours of the magnetic field lines.

We begin by examining Fig. 24. In Figs. 24(a) and 24(b), at 8.6 growth times, we are approximately at the saturation stage of the early nonlinear regime, where vortices would ordinarily develop. However, the magnetic tension resists vortex formation, resulting in filaments of enhanced vorticity and enhanced current density. The translational kinetic energy extracted from the flow is converted mostly into electromagnetic energy, with very little rotational energy, since the vortices fail to form. As shown in Fig. 24(b), this results in a deceleration of much of the flow, in particular, the regions of flow that perform the most work against the magnetic tension in the field lines, i.e., the background flow surrounding a narrow channel of high flow speed.

We continue to examine Fig. 24. There remains a central channel of maximum flow velocity ranging from $0.5\,c$ to $0.6\,c$, whose width is about $\frac{1}{5}$ the initial jet width, outside of which the flow speed drops abruptly to an average of about $0.3\,c$. The abrupt shear at the channel boundaries accounts for the central filaments of high vorticity. The outer high-vorticity filaments are produced by an abrupt shear in the background flow. However, this background flow is very heterogeneous, varying from about $0.2\,c$ to about $0.35\,c$. There is very close complementarity between the flow and magnetic field. As seen in Fig. 24(b), the field lines bend in response to the flow, and are concentrated where the flow exhibits rapid shear. This behavior gives rise to a large curl of the field, producing high-density current filaments. Certain field-influenced quantities (vorticity, current density, electromagnetic pressure, etc.) are enhanced by the direct conversion of bulk flow energy into

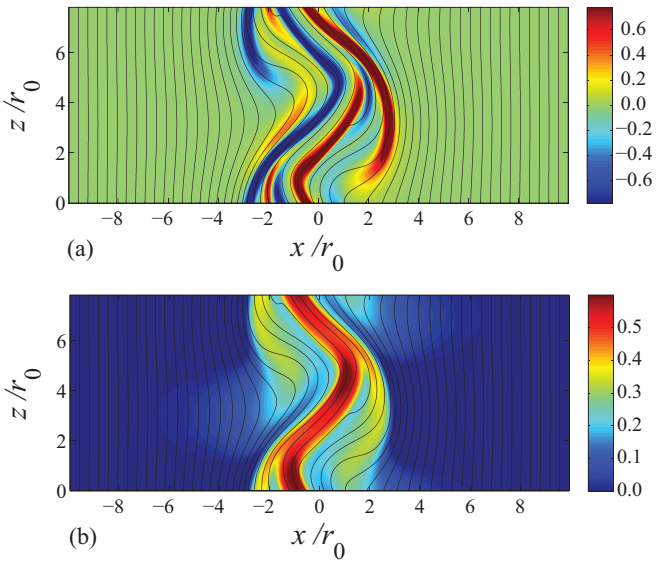

FIG. 24. (Color online) (a) Vorticity and (b) longitudinal velocity at $t = 8.62\,T_i = 4.93\,T = 117\,r_0/c$, where $M_A = 5.15$, $\beta_{\min} = 1.62$.

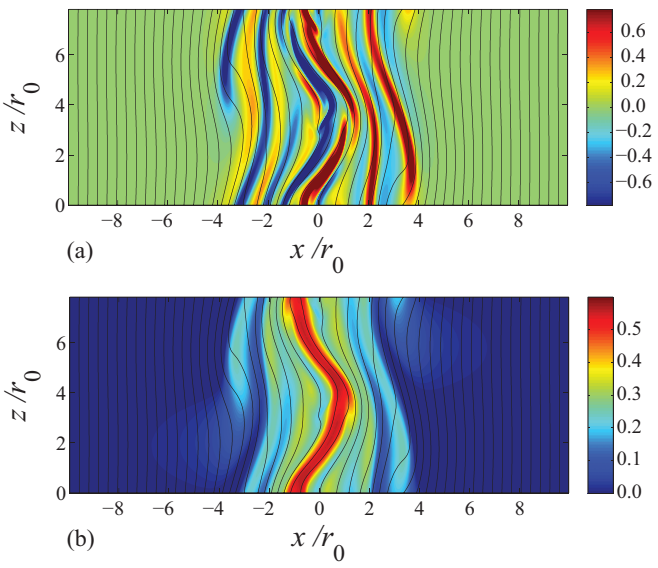

FIG. 25. (Color online) (a) Vorticity and (b) longitudinal velocity at $t = 13.2\,T_i = 7.52\,T = 178\,r_0/c$, where $M_A = 5.15$, $\beta_{\min} = 3.97$.

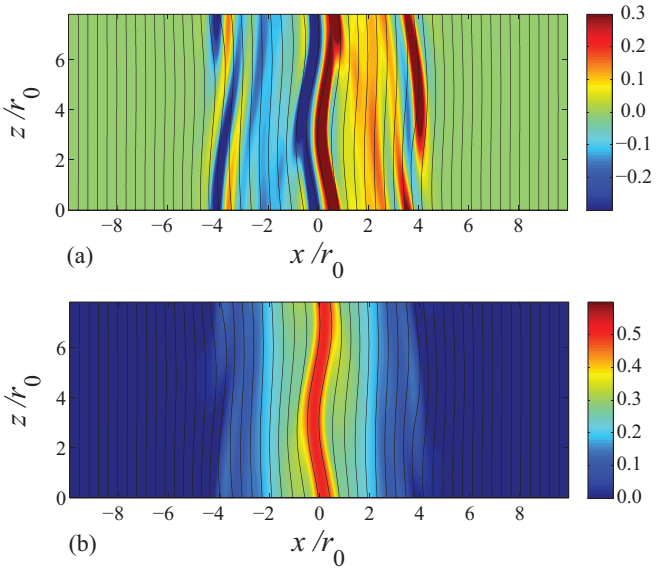

FIG. 26. (Color online) (a) Vorticity and (b) longitudinal velocity at $t = 21.8\,T_i = 12.5\,T = 295\,r_0/c$, where $M_A = 5.15$, $\beta_{\min} = 8.75$.

electromagnetic energy. Neither the vorticity in Fig. 24(a) nor the current density have yet reached their peak values. Both are still increasing.

However, the increase in electromagnetic energy is limited by the complete suppression of vortex formation since developing vortices would expel the field lines, providing further field amplification at the vortex boundaries. This is why, as we will see in Sec. VIII G, electromagnetic energy is not maximized for a strong vortex-suppressing field. Rather, vorticity and electromagnetic pressure are maximized for the strongest fields that still allow some vortex formation. This indicates that although the enhancement of these quantities is heavily dependent on the energy contained in the unperturbed field, this enhancement also has some dependence on field amplification due to vortex-induced centrifugal expulsion of field lines.

We return to the case $M_A = 5.145$, and progress to 13.2 growth times, for which the relevant displays are shown in Fig. 25. The vorticity and current density have already peaked, after about 10 growth times, and are now decreasing, as electromagnetic energy is now being viscously dissipated into thermal energy. From Fig. 25(a), the vortex and current filaments have become more closely aligned with the flow, and the jet has widened to about twice its initial width. There are now more filaments of alternating vorticity and alternating current density. The filaments alternate not only in the direction of vorticity (or current density) but also in the magnitudes of these quantities. That is, the vortex filaments in Fig. 25(a) alternate spatially between well-defined, narrow filaments of high vorticity, and less well-defined, viscously "smeared out" filaments of larger width and smaller vorticity in the opposite direction. The same happens with the current filaments. This is a striking manifestation of the viscous dissipation of electromagnetic and mechanical energy. The more sharply defined filaments have also narrowed, relative to Fig. 24(a), from $\frac{1}{5}$ of the initial jet width to only about $\frac{1}{8}$ the initial jet width. The vorticity is maximized around the narrow central flow region, which has also become more closely aligned with the flow direction. As shown in Fig. 25(b), the flow within this central channel has become more homogeneous, with a nearly uniform flow speed of $0.5\,c$. The background flow surrounding the central channel is still fairly heterogeneous, with flow speeds ranging from $0.2\,c$ to $0.3\,c$.

In Fig. 26, we see that after 21.8 growth times (note change in color scales, in order to preserve spatial contrast), the flow has relaxed to an equilibrium state in which the filaments are aligned with the flow direction, and the jet has further widened to about $8\,r_0$, or 2.25 times its initial width. As shown in Fig. 26(a), the vorticity and current density are now only about $\frac{1}{3}$ of their peak values. The filaments of relatively high vorticity (and current density) are now located at the left and right boundaries, and along the central axis. The enhanced vortex filaments have a width of about $0.6\,r_0$, i.e., $\frac{1}{6}$ of the initial jet width, while the current filaments are only about $\frac{1}{8}$ the initial jet width. Viscous dissipation has smeared the vorticity in the region between the central axis and the boundaries. This is likely due to the same mechanism discussed in the vortex-disruptive case. In particular, the vorticity has decreased by a factor of about 4, from its initial average value, and is now closer to the frequencies of modes associated with diffusion. The system therefore has a higher correlation with viscous processes, enabling a greater amount of energy transfer via viscous interactions. In Fig. 26(a), each filament of high vorticity corresponds to a pair of current filaments of alternating current density. A comparison of Figs. 26(a) and 26(b) shows that filaments of high vorticity correspond to locations of large and abrupt shear variation in the flow.

As shown in Fig. 26(b), the flow speed within the narrow central flow remains at a uniform value of $0.5\,c$. Since its formation in the early nonlinear regime, this central flow channel has maintained a nearly constant width of about $0.7\,r_0$, or $\frac{1}{5}$ the initial jet width, and corresponds to a narrow region of low density (i.e., a density undershoot, which we also observed in the vortex-disruptive case, but with a wider flow). Similar density undershoots were observed in the MHD simulation of Frank *et al.* [27] and the RMHD simulation of Mignone *et al.* [54]. This narrow central flow region occurs for stronger fields ($M_A = 5.145$ and 10.3), and is a consequence of the field lines having sufficient magnetic tension to extract large amounts of electromagnetic energy directly from the translational kinetic energy of the flow, without allowing more of this energy to be diverted into the rotational kinetic energy of developing vortices. Surrounding this narrow central flow is a region in which the flow speed is about $0.3\,c$ and whose width is very nearly equal to the initial flow width (about $3.6\,r_0$). The background flow is also much more homogeneous than at earlier times. These same flow properties are also observed in the equilibrium state of the strongly vortex-disruptive field $M_A = 10.3$ (see Fig. 23). As with the weaker vortex-disruptive fields, the system has relaxed to an equilibrium configuration which retains a memory of its initial configuration. In the initial jet, and the equilibrium configurations of vortex-disruptive and vortex-suppressing fields, we have vortex filaments of positive vorticity to the right of the axis, and filaments of negative vorticity to the left of the axis, along with flow velocity falling off with distance from the central axis, asymptotically approaching zero. However, unlike the vortex-disruptive case $M_A = 41.4$, the relaxation to equilibrium occurs after about 20 growth times, whereas in the $M_A = 41.4$ case, equilibrium still has not been reached after 60 growth times. There is also greater enhancement of vorticity, along the axis and at the boundaries, for the vortex-suppressing case than the vortex-disruptive cases. Only the vortex-suppressing case, and the strongly vortex-disruptive case $M_A = 10.3$, contain a narrow central region that retains high flow speed. Only the vortex-suppressing case develops a background flow region of uniform flow speed whose width very nearly coincides with the width of the initial jet, as shown in Fig. 26(b). Thus, we see that when vortices are completely suppressed, the system retains not only a qualitative but also a quantitative memory of the initial flow.

We see that maximum flow deceleration, from $0.7\,c$ to about $0.2\,c$, occurs for the intermediate vortex-disruptive fields $M_A = 41.4$ and 20.7, whereas the stronger fields only decelerate the jet to about $0.4\,c$ ($M_A = 10.3$) or $0.5\,c$ ($M_A = 5.13$). The intermediate vortex-disruptive fields allow a sufficient amount of vortex development to result in a complex reorganization process associated with vortex disruption, partly driven by extensive magnetic reconnection. This maximizes the complexity and number of smaller-scale structures arising

from turbulent breakdown, which in turn enhances the amount of correlation with the small length scales set by diffusion. This maximizes the viscous dissipation of mechanical energy into thermal energy. For stronger fields, there is less dissipation, and the residual mechanical energy is concentrated in a narrow central flow channel. For weaker fields (e.g., $M_A = 82$), vortex disruption is too gradual, and the emergent features are dissipated before they have the opportunity to interact in a turbulent manner.

Having examined two-dimensional displays of our simulation results, in the next section we wish to further illuminate these results by examining plots, versus time, of certain spatially averaged or maximized quantities.

G. Bifurcations in energy transfer

We have observed several bifurcations in the mechanisms of energy transfer during nonlinear evolution, which is to say, certain energy-transfer processes are optimized at intermediate field strengths. We observed the first such bifurcation in the viscous dissipation of mechanical and electromagnetic energy into thermal form, which is optimized for intermediate vortex-disruptive fields. We see this more explicitly in Fig. 27, which shows the time dependence of the (a) average longitudinal velocity and (b) average pressure. As the field strength increases from $M_A = 82$ to 41 and 21, the average longitudinal velocity decreases in the latter nonlinear regime, and the average pressure correspondingly increases. However, as the field strength continues to increase to $M_A = 10.3$ and 5.1, the average longitudinal velocity now increases, and the average pressure decreases. That is, the longitudinal velocity is minimized, and the pressure maximized, for the intermediate fields $M_A = 41$ and 21.

As we have seen, these field strengths allow fairly extensive vortex formation, which is followed by sufficiently rapid vortex disruption to lead to a complex turbulent regime. The small length scales of these turbulent structures are comparable to length scales set by diffusion. Furthermore, the turbulent structures have much smaller vorticity (only about $\frac{1}{4}$ of the value at the amplification stage), and this vorticity is more comparable to the frequencies associated with diffusion. The resulting turbulent evolution is therefore closely correlated with viscous dissipation into thermal energy (seen in the maximized thermal pressure), and consequent deceleration of the jet (seen in the minimized longitudinal velocity). Turbulence also diverts the directional energy of the bulk flow into random motions, which maximizes the longitudinal deceleration. Stronger fields (e.g., $M_A = 10.3$ and 5.1) do not allow sufficient vortex development to lead to a complex turbulent regime, and therefore viscous dissipation is not as great. In these strong-field cases, the residual mechanical energy is concentrated in a narrow central flow channel. For weak fields ($M_A = 82$), the vortex disruption is too gradual, and therefore the emergent features are dissipated before they can interact with one another in a turbulent manner. This bifurcation is also observed in plots of the root-mean-squared (RMS) and maximum Lorentz factor versus time. The bifurcation is not observed, however, in the RMS and maximum *transverse* velocity. The transverse motions are correlated with vortex development and jet broadening, both of which are increasingly suppressed for stronger fields.

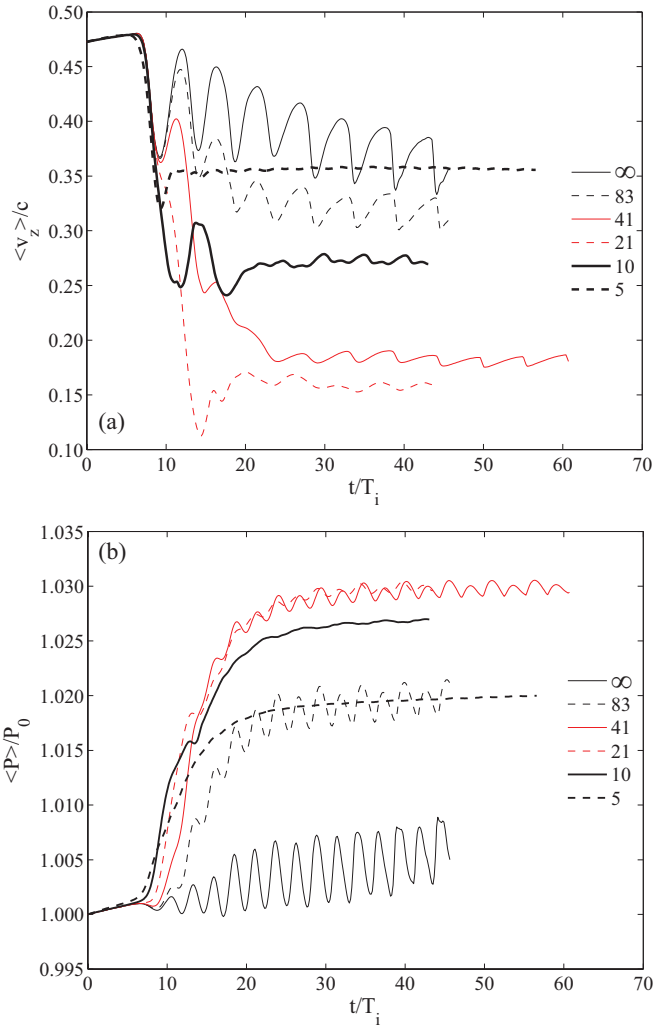

FIG. 27. (Color online) Average (a) longitudinal velocity and (b) pressure vs time at different field strengths, where M_A is labeled above.

Figure 27 also shows nonlinear oscillations in the curves corresponding to the weaker fields $M_A = 82$, 41, and 21. However, these oscillations are suppressed for the stronger fields $M_A = 10.3$ and 5.1. The oscillations are caused by a pair of nonlinear transverse acoustic waves which propagate between the jet axis and transverse boundaries. Although the system width has an influence on the period of these acoustic waves, it does not significantly influence the evolution of the flow and its interaction with the magnetic field, as we have verified by comparing results for two different system widths. Fields for which $M_A < 20$ are strong enough not only to suppress complex turbulent breakdown and viscous dissipation, as described above, but also to suppress nonlinear acoustic waves. The unperturbed flow speed in these cases is $0.7\,c$ along the central axis. For less relativistic flow speeds, these oscillations have smaller amplitude, and for nonrelativistic flows, the oscillations are barely noticeable. These acoustic waves are therefore a relativistic effect.

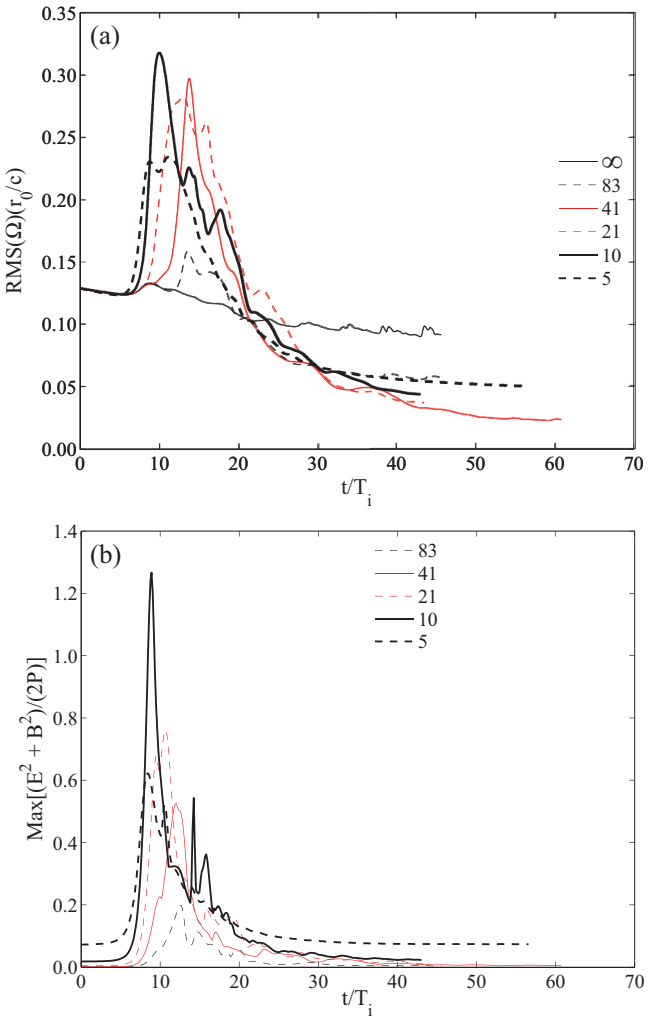

FIG. 28. (Color online) (a) RMS vorticity vs time and (b) max. EM to thermal pressure (relative to unperturbed value) vs time at different field strengths, where M_A is labeled above.

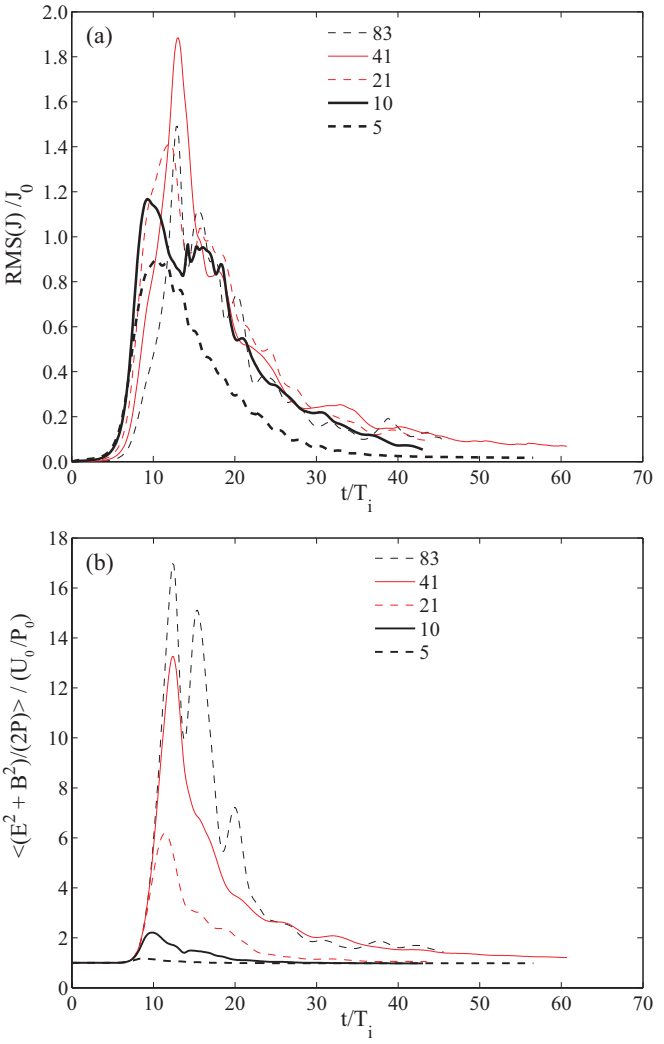

FIG. 29. (Color online) (a) RMS current density and (b) average. EM pressure amplification vs time at different field strengths, where M_A is labeled above.

The second bifurcation pertains to the electromagnetic (EM) energy in the early nonlinear regime, which reaches its largest values for strong vortex-disruptive fields, that is, fields which are strong enough to suppress vortex development and turbulent breakdown, but not strong enough to completely suppress vortex formation. Among the fields sampled, this corresponds most closely to the field $M_A = 10.3$, as shown in the plots in Fig. 28, which shows the (a) RMS vorticity and (b) maximum electromagnetic pressure as functions of time. Both quantities, as with other quantities related to field strength, reach a peak in the early nonlinear regime, followed by gradual decay that asymptotically approaches a small equilibrium value. In both plots, we see that as field strength increases through the vortex-disruptive regime (from $M_A = 82.8$ to 10.3), the peaks increase in height. However, for the vortex-suppressing field $M_A = 5.1$, the peaks are considerably smaller. This means that, although the amount of electromagnetic energy in the flow is heavily dependent on unperturbed field strength, maximization of electromagnetic energy requires some field amplification through vortex formation. This is seen by the smaller peak values for the vortex-suppressing field. That is to say, higher electromagnetic energies are reached when some of the bulk flow energy is diverted into rotational form, allowing diffusion of the field lines into partially formed vortices. This same argument applies to maximization of related quantities such as electromagnetic momentum and vorticity.

As shown in Fig. 29(a), the current density also exhibits an early peak followed by a gradual decay. However, the peak current density is maximized for the weak vortex-disruptive field $M_A = 41$. This is because current density is the curl of the field, and therefore is dependent not so much on the field strength as on the shear in the field strength. Maximum shear occurs through concentration of the field lines, which requires fairly extensive vortex formation, and therefore a weak vortex-disruptive field. Also, whereas maximum electromagnetic energy is achieved for strong vortex-disruptive fields, maximum *amplification* of electromagnetic energy, relative to its initial value, is achieved for the weakest fields, as shown in Fig. 29(b). That is, field amplification is proportional to the amount of vortex development, and therefore decreases with increasing field strength. So, although there is a bifurcation

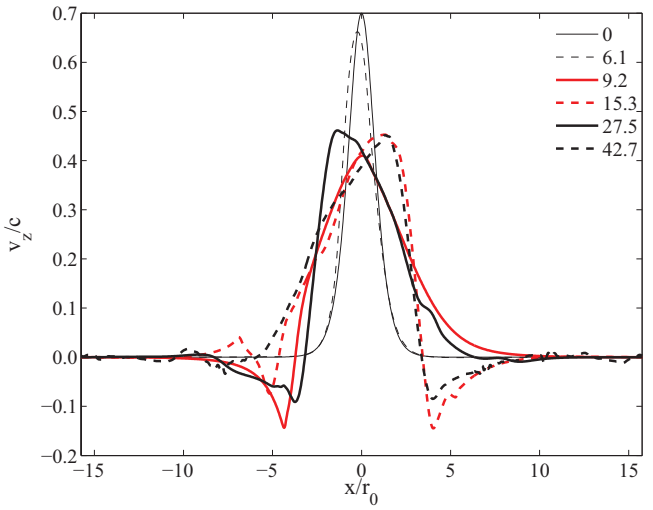

FIG. 30. (Color online) Longitudinal velocity vs x/r_0 at $z = 0$ for unmagnetized case at times listed above in units of growth time.

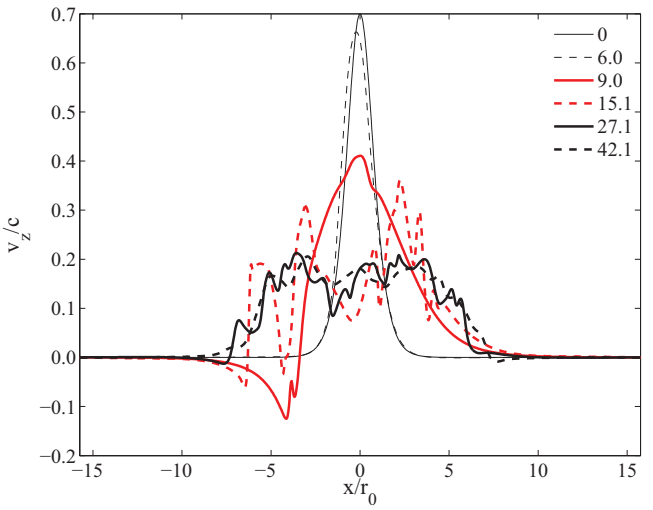

FIG. 32. (Color online) Longitudinal velocity vs x/r_0 at $z = 0$ for $M_A = 21$ at times listed above in units of growth time.

in the amount of electromagnetic energy extracted, there is no such bifurcation in the amplification of electromagnetic energy relative to its unperturbed value.

In the next section, we further explore certain quantitative aspects of the evolution of the flow.

H. Properties of the flow evolution

Here, we further illuminate certain quantitative properties of the flow evolution for the field strengths studied, first by presenting cross sections of longitudinal flow speed, and then by presenting graphs of the spatially averaged relativistic Alfvénic Mach number M_A as a function of time. We do each of the above for the different field strengths studied. First, for each field strength, including the unmagnetized case, we display cross sections of the longitudinal flow speed at $z = 0$ for a set of successive times in the simulation (in units of the growth time T_i). These are shown in Figs. 30 through 34. In each case, the profile at time $t = 0$ is the sech^2 profile given in Eq. (4).

We first examine Fig. 30, which corresponds to the unmagnetized case. Here, we see that the flow speed amplitude rapidly decreases during the linear evolution (prior to about nine growth times) from $0.7\,c$ to an equilibrium value of roughly $0.5\,c$. The curves also lose their symmetry due to the emergence of the primary vortices, where the location of the velocity peak (to the left or right) is determined by the nature of the vortical behavior at $z = 0$ at the time being plotted. The vortices also cause backflow which results in the negative flow speeds seen at the boundaries of the profiles. The presence of negative flow speeds well into the nonlinear evolution is a sign that the vortices persist in the absence of a magnetic field. The profiles have also broadened to about four times the initial flow width, which is comparable to the amount of broadening observed for a weak field, as in Fig. 31. This indicates that much of the jet broadening observed

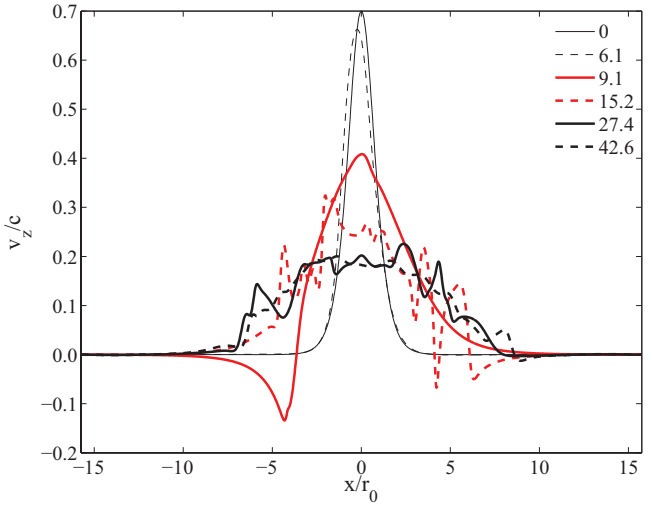

FIG. 31. (Color online) Longitudinal velocity vs x/r_0 at $z = 0$ for $M_A = 41$ at times listed above in units of growth time.

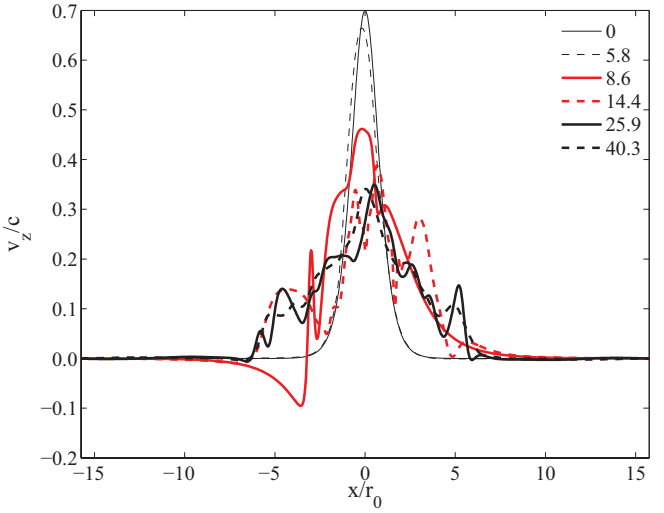

FIG. 33. (Color online) Longitudinal velocity vs x/r_0 at $z = 0$ for $M_A = 10$ at times listed above in units of growth time.

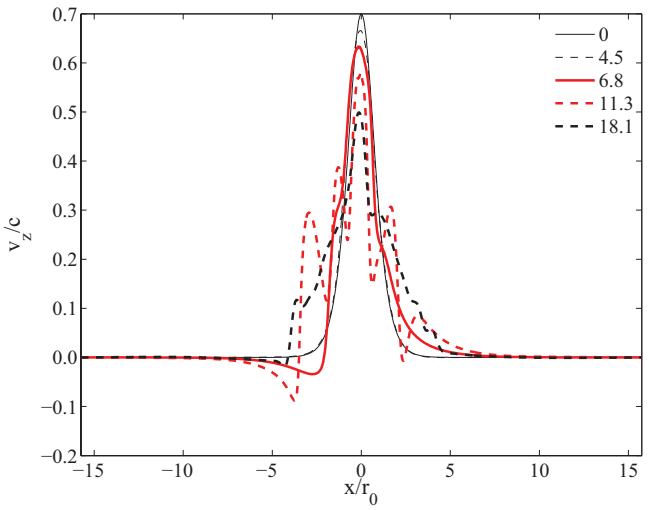

FIG. 34. (Color online) Longitudinal velocity vs x/r_0 at $z = 0$ for $M_A = 5.1$ at times listed above in units of growth time.

in the displays is a consequence of vortex formation, and turbulent vortex inhibition by the field contributes relatively little additional broadening. We also see that flow deceleration, probably through viscous dissipation, begins in the linear regime, and does not require vortex formation or turbulent interaction with a magnetic field.

We now examine Fig. 31, corresponding to the relatively weak vortex-disruptive field $M_A = 41$. Again, much of the flow deceleration, from $0.7\,c$ to $0.4\,c$, occurs during the linear regime. The curves corresponding to fewer than 10 growth times are quite similar to those in Fig. 30, indicating that prior to the point of field amplification by the vortices, the magnetic field has little influence on the evolution. The curve at $15.2\,T_i$ exhibits rapid fluctuations, corresponding to a transition to a turbulent regime as the vortices are almost completely inhibited. In the later stages of the nonlinear evolution, the thick black curves have a more regular shape, and a central flat region, consistent with our previous observation in the displays of the formation of a fairly homogeneous central flow corresponding to a central region of persistent vortical activity. We also observe deceleration to a flow speed of about $0.2\,c$, consistent with turbulent dissipation of mechanical energy for weak vortex-disruptive fields. The presence of a backflow region (a region of negative flow speeds) at $9.1\,T_i$ indicates the presence of vortices at this time. The lack of a backflow in the other curves indicates that at these times the vortices have either not formed or have been inhibited.

We now examine Fig. 32, corresponding to the intermediate vortex-disruptive field $M_A = 21$. The first three curves show that the linear and early nonlinear evolution, prior to $10\,T_i$, is similar to the previous two cases. The presence of a backflow region at $9.0\,T_i$ indicates the presence of vortices at this time, but not at the other times plotted, as these curves do not have backflow regions. The fluctuations in the curve at $15.1\,T_i$ indicate turbulent reorganization similar to that observed for $M_A = 41$. The thick black curves show a deceleration to $0.2\,c$, as with $M_A = 41$, as equilibrium is approached. However, these late evolution curves exhibit more fluctuation than the corresponding curves for $M_A = 41$, which is consistent with our observation from the displays that the central flow region is more homogeneous for $M_A = 41$ than for $M_A = 21$. There, amount of broadening of the flow is comparable to that observed for the unmagnetized case.

The curves in Fig. 33 correspond to the strong vortex-disruptive field $M_A = 10$. There is less flow deceleration than in the weaker field cases, as the flow speed amplitude remains above $0.3\,c$ as equilibrium is approached, and less broadening of the flow. This is consistent with our observations from the displays that this field inhibits the vortices while partially formed, which therefore reduces the amount of vortex twisting of field lines, magnetic reconnection, turbulent reorganization, and hence viscous dissipation of mechanical energy into thermal energy. The residual mechanical energy is contained in a central channel, seen previously in the longitudinal velocity displays and here in the central velocity peaks in the curves corresponding to later evolution. These velocity peaks are not present in the late evolution curves for the weaker fields. These curves also exhibit less fluctuation, consistent with the reduced amount of turbulence.

The curves in Fig. 33 correspond to the vortex-suppressing field $M_A = 5.1$. We see that in the absence of vortex formation, the central flow peak remains very pronounced, and remains above about $0.45\,c$ well into the nonlinear evolution, at times much larger than $18.1\,T_i$. The curves also show much less broadening and reduced turbulent fluctuations. We see how closely these phenomena are associated with vortex formation and interaction with weak fields.

We now examine the time evolution of the spatially averaged relativistic Alfvénic Mach number for each of the unperturbed values of M_A in this study. When we refer to a simulation as corresponding to a given value of M_A, whether 41, 21, 10, or 5, this refers to the unperturbed value calculated using Eq. (13) from the initial unperturbed values of the quantities. We can, however, also define an instantaneous value of this parameter at a given time and location as follows:

$$M_A(x,z,t) = \frac{v(x,z,t)\gamma(x,z,t)}{v_A(x,z,t)\gamma_A(x,z,t)}, \tag{22}$$

where

$$\begin{aligned} v(x,z,t) &= \sqrt{v_x(x,z,t)^2 + v_z(x,z,t)^2}, \\ v_A(x,z,t) &= \frac{\sqrt{B_x(x,z,t)^2 + B_z(x,z,t)^2}}{\sqrt{w(x,z,t)}}, \\ \gamma(x,z,t) &= \frac{1}{\sqrt{1 - v(x,z,t)^2/c^2}}, \\ \gamma_A(x,z,t) &= \frac{1}{\sqrt{1 - v_A(x,z,t)^2/c^2}}, \\ w(x,z,t) &= \rho(x,z,t) + \frac{\Gamma}{\Gamma - 1} P(x,z,t) \\ &= \rho(x,z,t) + 4\,P(x,z,t). \end{aligned} \tag{23}$$

In Fig. 35, we present the spatially averaged value of $M_A(x,z,t)$ as a function of time for a set of representative field strengths corresponding to unperturbed initial M_A of 82, 41, 21, 10, and 5, in order of increasing field strength. The periodic oscillations are due to oscillations in the flow speed, caused by boundary reverberations of transverse acoustic waves, which

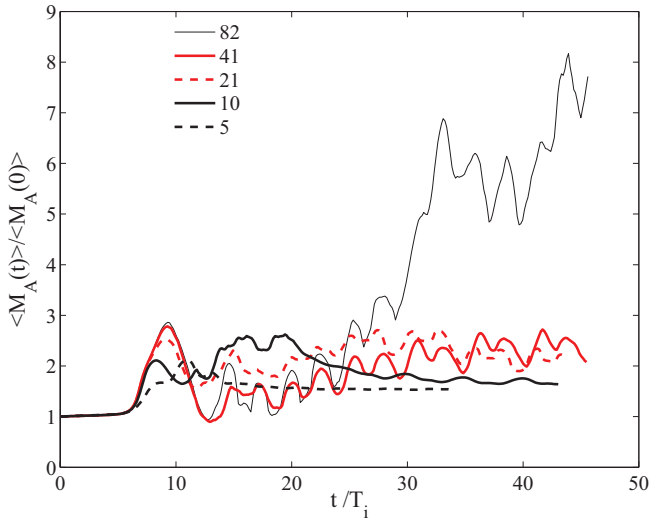

FIG. 35. (Color online) Spatially averaged relativistic Alfvénic Mach number $\langle M_A \rangle$ vs t/T_i for unperturbed values of M_A listed above. The average M_A are scaled relative to their average values at $t = 0$, and these initial average values scale with the unperturbed values of M_A.

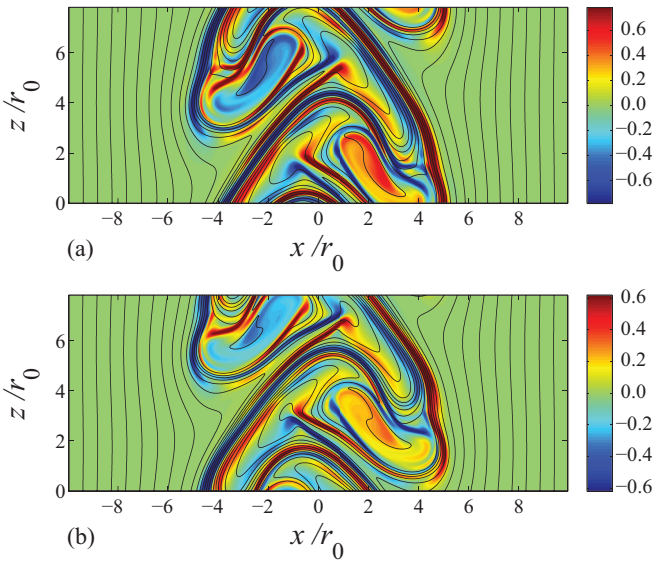

FIG. 36. (Color online) Vorticity at (a) $v_{z0} = 0.7\,c$ and (b) $v_{z0} = 0.5\,c$, where $M_A = 20.7$ and $t = 12.2\,T_i$.

we have shown does not significantly influence the evolution of the flow. These oscillations are suppressed for stronger field strengths. For weaker fields, we see that $\langle M_A \rangle$ increases more rapidly with time, and at later times is at a larger multiple of its initial value. For stronger fields, $\langle M_A \rangle$ tends more quickly toward an equilibrium value which is about 1.5 times its initial value. This trend is consistent with the tendency of stronger fields to suppress intermediate turbulent behavior and produce a rapid transition to an equilibrium filamented state.

For lower values of the initial M_A, $\langle M_A \rangle$ at later times is a smaller multiple of its initial value. There are two factors involved in this trend. The intermediate fields $M_A = 41$ and 21 correspond to maximum deceleration of the central flow, discussed in Sec. VIII G, resulting in less amplified equilibrium values of $\langle M_A \rangle$ than for the weaker field $M_A = 82$, for which there is much less deceleration of the flow. Figure 35 shows that for $M_A = 41$ or 21, $\langle M_A \rangle$ is only amplified by a factor of about 2. For the stronger fields $M_A = 10$ and 5, the equilibrium values of $\langle M_A \rangle$ are even less amplified (only 1.5 times the initial value). Although the flow deceleration is not as great for these cases, the tension in the magnetic field lines is able to maintain the magnetic field strength during the transition to equilibrium, thereby minimizing the amplification of $\langle M_A \rangle$.

Another feature of interest, particularly for the weaker fields, are the early peaks in $\langle M_A \rangle$ after about 10 growth times, followed immediately by troughs at about 12 growth times. The early peaks correspond to the initial formation of the large primary vortices immediately after saturation. The rapid fluid circulation within the vortices increases the average flow speed, thereby increasing $\langle M_A \rangle$. For stronger fields, which more rapidly suppress vortex formation, these peaks are not nearly as evident. The troughs at about 12 growth times correspond to field amplification through centrifugal expulsion of field lines by the rotating vortices. This amplification of field strength causes a decrease in $\langle M_A \rangle$. This feature, also, is more pronounced for the weaker-field cases, for which there is greater vortex twisting of the field lines, and therefore greater concentration of centrifugally expelled field lines.

Unless otherwise noted, M_A is given by Eq. (13), and corresponds to initial unperturbed quantities. We now proceed to verify that, for a given value of M_A, the results exhibit little dependence on flow speed.

I. Importance of the parameter M_A

In this section, we consider a given value of M_A and compare numerical results for two different unperturbed flow speeds. We consider the field corresponding to $M_A = 20.7$, and unperturbed flow speed amplitudes of $0.7\,c$ and $0.5\,c$. Because these two cases have the same M_A but different flow speeds, they also have different values of the Alfvén speed v_A, the plasma β, and the linear growth rate ω_i. The growth time is $T_i = 1/\omega_i = 10.2\,r_0/c$ at $0.7\,c$ and $T_i = 13.4\,r_0/c$ at $0.5\,c$. Figure 36 shows the vorticity displays for each flow speed after 12.2 growth times. As the figures illustrate, the results exhibit close agreement well into the nonlinear evolution. The most noticeable difference is a longitudinal shift arising from the difference in pattern speeds. Close agreement between flow speeds is seen in each value of M_A studied [63]. This demonstrates that within a regime of moderately relativistic unperturbed flow speeds (between about $0.25\,c$ and $0.8\,c$), the influence of the magnetic field is governed not by flow speed, Alfvén speed, or the plasma β, but instead by the parameter M_A, our relativistic extension of the Alfvénic Mach number, as we have defined it in Eq. (13). Furthermore, the agreement occurs after a given number of growth times $T_i = 1/\omega_i$, as opposed to clock times, periods, sound transit times, Alfvén transit times, etc. The growth time is therefore the most reasonable unit for characterizing the time dependence of the evolution.

We now verify that, to a high degree of numerical accuracy, the vorticity satisfies a certain condition of alternating symmetry.

J. Alternating symmetry of vorticity

We notice throughout our vorticity displays that the vorticity satisfies a certain condition of alternating symmetry, which is dictated by the symmetry of the unperturbed velocity profile and the antisymmetry of the pressure perturbation profiles. Specifically, we have equal and opposite vorticity on either side of the central axis at locations separated by half the longitudinal perturbation wavelength. If we denote the vorticity $\Omega(x,z,t)$, then mathematically, this condition reads as

$$\Omega(x,z,t) = -\Omega(-x,z+\lambda/2,t), \tag{24}$$

where $\lambda = 2\pi/k_z$ is the wavelength of the initial perturbation. This condition is a mathematical interpretation of the half-wavelength separation of counter-rotating vortices that form in the early nonlinear evolution, but is maintained throughout the evolution, in both the magnetized and unmagnetized cases. The accuracy with which this condition is satisfied provides a measure of the numerical accuracy of our results. Specifically, we compute the ratio

$$f = \frac{|\Omega(x,z,t) + \Omega(-x,z+\lambda/2,t)|}{|\Omega(x,z,t)|}. \tag{25}$$

The average value of this ratio is roughly 10^{-5} during the nonlinear evolution of a magnetized case. This provides one method of validation of the numerical accuracy of our simulations.

We have examined the evolution of the flow for a wide range of unperturbed field strengths. However, all of these fall within roughly an order of magnitude of one another, which falls within the uncertainty in estimates of magnetic field strength of astrophysical jets, obtained from synchrotron emission observations. It is therefore of interest to identify potential applications of our simulation results to various observed jets, which we proceed to do in the next section.

K. Comparison with jet observations

In this section, we offer potential applications of our simulation results to jet observations. However, we do not make any claims as to the accuracy or completeness of our model in describing the physical mechanisms behind any of the jets mentioned. Other mechanisms (e.g., radiative cooling, jet precession) are undoubtedly present.

Several extragalactic jets show qualitative agreement with vortex formation, followed by vortex inhibition by a disruptive magnetic field (including M87, Centaurus A, 3C 120, 3C 273, HH 30, HH 49, etc.). Closer to the nucleus, we often observe features resembling vortices. This is often followed by a disruptive stage in which these features break into smaller-scale structures, qualitatively resembling vortex disruption and turbulent breakdown. Filaments are observed in such jets as M87 [64], 3C 273 [19], and 3C120 [17,18]. These might be produced by vortex shedding during the disruptive stage, or might be associated with the dual filamentary structure connecting the vortices throughout their development. Many images also show significant jet widening, consistent with the widening observed in the simulations. In the outer regions of the jet, this widening seems to be coupled with the viscous dissipation and flow deceleration also observed in the simulations. Note that for the model we are using, a magnetic field is required in order to qualitatively reproduce these observed features. In particular, the field should be vortex disruptive, and not vortex suppressing, since the features are closely correlated with the stages of vortex inhibition. In the absence of a magnetic field, the simulation predicts that the vortices persist almost indefinitely.

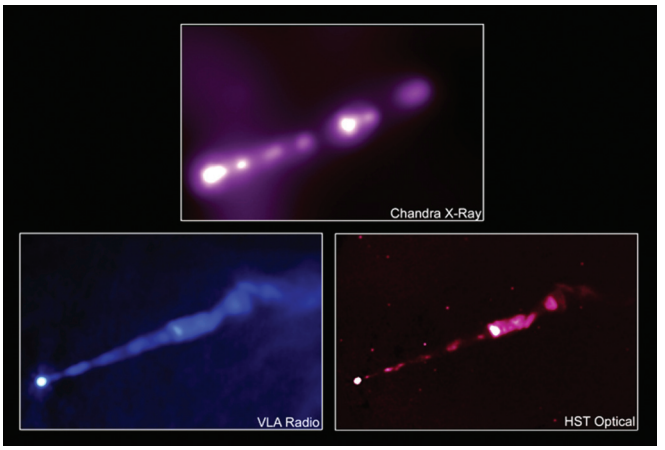

FIG. 37. (Color online) Extragalactic jet M87 (aka Virgo A, NGC 4486).

Figure 37 shows three images of the extragalactic radio jet M87, also known as Virgo A, and NGC 4486 (this figure was taken from http://apod.nasa.gov/apod/ap011101.html). The x-ray image is produced by Chandra, the radio image by the VLA (very large array), and the optical image by the Hubble Space Telescope. M87 is a highly energetic plasma jet extending 1.5 kpc, and which emanates from a supermassive central black hole in a supergiant elliptical galaxy. As in our simulations, the unperturbed magnetic field is believed to be primarily aligned with the flow [64]. However, in certain knots (i.e., knot A and knot C), the field is believed to be primarily transverse to the flow [64], which might be consistent with vortex twisting of field lines within these knots, resulting in field amplification. Stawarz *et al*. [65] estimated an amplified field of at least 300 μG within knot A, where the field elsewhere in the jet is believed to be less than about 100 μG, as discussed in Hines *et al*. [64]. So, the knots may indeed behave like vortices, twisting the magnetic field lines into partially transverse configurations, and centrifugally expelling them to the vortex extremities, resulting in field amplification. Furthermore, the field outside the knots is believed to be aligned with the flow [64], which is the unperturbed field configuration used in our numerical simulations.

Whereas our simulation displays show the behavior of the flow at a sequence of time steps, Fig. 37 shows a view of an entire jet, which is to say, multiple stages of evolution in a single image. As our numerical simulation box progresses forward in time, we can think of our simulation box moving outward along the axis of the jet, away from the central nucleus.

It should be emphasized that these comparisons only suggest possible physical mechanisms that might offer insight into the observed jet features. Other mechanisms (radiative cooling, etc.) are undoubtedly present. Another important point is that the field strengths examined in our study are separated

by roughly an order of magnitude, which falls well within the uncertainty in estimates of field strength in astrophysical jets. These estimates are obtained from synchrotron emission observations.

We now proceed to summarize the salient conclusions of our study.

IX. CONCLUSION

We have examined the evolution of the KH instability in a relativistic magnetized sheared plasma flow. We did this by numerically solving the single-fluid RMHD equations of Anile [51] in conservative form, using a method which is fourth order in both space and time, and which uses the highly accurate, rapidly convergent algorithm of Newman [26] to recover the primitive variables from the conserved quantities in the RMHD equations. The exact single-fluid equations are marginally stable, but become unstable when discretized in a numerical scheme. We therefore used numerical viscosity to restore stability to the system. In explicit finite-differencing schemes, viscosity is implicitly present in second order. The use of fourth-order methods gives us explicit control over the viscosity coefficients.

Our simulation results show good convergence with respect to time step, spatial step, system dimensions, viscosity, and between the RHD, MHD, and RMHD regimes. Each magnetic field remains approximately divergenceless throughout the evolution, and the vorticity satisfies the condition of alternating symmetry to a high level of accuracy, as shown in Sec. VIII J. When we speak of convergence with respect to the longitudinal dimension, we mean that the results are essentially unaffected by the number of perturbation wavelengths spanned by the system in the longitudinal direction. There are nonlinear transverse acoustic waves whose oscillation period is affected by the transverse system width. However, we have shown that this does not in turn significantly influence the evolution of the flow and its interaction with the magnetic field. Therefore, the evolution is convergent with respect to system width. Further detail of this is provided in Hamlin [63].

In several respects, we have convergence between the HD, RHD, MHD, and RMHD regimes. The linearization of the single-fluid equations yields a second-order ODE, given by Eq. (10) in Sec. V, which has the same underlying structure in all four regimes [63]. We have also verified that the nonlinear simulation results are convergent between the four regimes [63], as are the results for the linear growth rates [63]. These demonstrations are provided in more detail in Hamlin [63].

In the absence of a magnetic field, we found KH-unstable vortices, connected by a dual filamentary structure, which persist well into the nonlinear regime. When a magnetic field is present, the vortices are inhibited through a series of stages. Aspects of these stages are discussed in classical MHD literature [27–29,38]. We have examined in detail how and to what extent these stages manifest in RMHD for a set of representative field strengths. We have found that the influence of the magnetic field is strongly correlated with a relativistic extension of the Alfvénic Mach number M_A, which we have defined, in Eq. (13), analogously to the manner in which Bodo *et al*. [31] defined a relativistic extension of the sonic Mach number. As we saw in Sec. VI B, the fractional reduction in linear growth rate is closely correlated with M_A. For each value of M_A studied, we have also compared our simulation results at two different unperturbed flow speeds, $0.7\,c$ and $0.5\,c$, and found that the results maintain close similarity well into the nonlinear regime of evolution. This demonstrates that within a regime of moderately relativistic flow speeds (v_{z0} between approximately $0.25\,c$ and $0.8\,c$), the parameter M_A indeed has a close correlation with the influence of the magnetic field on the flow.

The stages of vortex inhibition are as follows. First, the rotating vortices centrifugally expel the field lines to the vortex extremities, so that they become concentrated in external connective filaments, resulting in amplified field in these filaments. The vortices twist the field lines as they rotate, resulting in magnetic reconnection. The field lines in turn exert magnetic stresses on the vortices, which halt their rotation, and result in vortex deformation and shedding of amplified filamentary features. This is the disruptive stage. The vortices then undergo reconnection-driven turbulent breakdown into small-scale structures, resulting in jet deceleration and broadening as energy is viscously dissipated. Finally, the system relaxes to an equilibrium configuration in which the field lines and vortex filaments are aligned with the flow direction. Vortex disruption corresponds to a disruption of the faster-moving components of the flow, leaving behind the slower-moving background flow.

For all field strengths studied, there is remarkable complementarity between the flow and the magnetic field, seen in the overlays of the field lines onto color displays of the vorticity and longitudinal flow. This complementarity can be viewed in terms of an interaction between mechanical energy and electromagnetic stresses. When the vortices form shortly after saturation, the flow initially drives the field, through field amplification by centrifugal vortex expulsion of field lines, and subsequent twisting of the field lines through vortex rotation. Then, the field builds up sufficient electromagnetic stresses to constrain the flow, as the tension in the field lines halts vortex rotation while deforming and disrupting the vortices. Vortex behavior also leads to magnetic reconnection, which in turn enhances the turbulent breakdown of the faster-moving components of the flow.

In general, for stronger unperturbed fields, there is more rapid vortex inhibition, less magnetic reconnection, less jet broadening, and a more rapid transition to an equilibrium flow-aligned state. Sufficiently strong fields ($M_A < 6$) suppress vortex formation altogether, resulting in an immediate transition to an equilibrium state. For the weakest vortex-disruptive fields (e.g., $M_A = 82$), there is extensive jet broadening due to extensive vortex development. However, vortex disruption is very gradual, and the emergent features are viscously dissipated before they have the opportunity to interact in a turbulent manner that enhances the viscous dissipation. Therefore, weakly vortex-disruptive fields do not optimize the viscous dissipation of mechanical energy into thermal energy, i.e., jet deceleration. This energy transfer is optimized for intermediate vortex-disruptive fields, in the range $20 \leqslant M_A \leqslant 42$. These fields are weak enough to allow sufficient vortex development, and magnetic reconnection, for a turbulent regime, but also strong enough for rapid vortex disruption, which enables strong interaction of the emergent features.

Viscous dissipation can also be explained in terms of length scales and frequencies. Small-scale turbulent features have small length scales which are more comparable to the length scales imposed by diffusion. As the vorticity of the system decreases over time, it becomes more comparable to the frequencies of modes introduced by diffusion. These processes enhance the coupling of the evolution to viscous dissipation.

Fields which are stronger than this ($M_A < 20$) do not allow sufficient vortex development and magnetic reconnection to enable a complex turbulent breakdown, and the amount of viscous dissipation is reduced. The residual mechanical energy of the flow is concentrated in a narrow central flow channel which is characteristic of strong vortex-disruptive and vortex-suppressing fields. This channel corresponds to a region of low density. Low-density channels were also observed in the simulations of Frank *et al.* [27] and Mignone *et al.* [54]. For strong fields, viscous dissipation is probably caused primarily by a decrease in vorticity over time, which then becomes more comparable to modal frequencies associated with diffusion. In the vortex-suppressing case $M_A = 5.15$, the central flow channel is surrounded by a background flow whose width is almost identical to the initial jet width, which indicates that for fields of this strength, the system retains not only a qualitative but also a quantitative memory of its initial configuration.

We also found that maximum values of quantities related to electromagnetic energy, in the early nonlinear regime, are reached for the strongest fields which still allow partial vortex formation. For fields which suppress vortex formation, maximum electromagnetic energy is significantly reduced. Therefore, while the amount of electromagnetic energy is heavily dependent on the strength of the unperturbed field, the maximization of peaks in electromagnetic energy, electromagnetic momentum, and vorticity require some amount of field amplification by vortex-induced centrifugal expulsion of field lines. The current density, however, is optimized for weaker vortex-disruptive fields ($M_A = 41.4$). This is because the current density is the curl of the magnetic field, and therefore is proportional not to the field strength itself but to the shear in field strength, which is maximized when field lines are concentrated through vortex-induced expulsion.

The magnetic fields studied are within about an order of magnitude of one another in strength, which is within the range of uncertainty in field estimates of astrophysical jets, as inferred from synchrotron emission data. Therefore, one potential application of our results is in relation to observations of astrophysical jets. We find qualitative similarities with observations of numerous jets, including M87, Centaurus A, 3C 273, and 3C 120, in terms of possible vortex formation followed by turbulent breakdown, filamentation, and jet broadening. In particular, some of the knots in M87 have amplified fields (at least 300 μG [65]), which have transverse components [64] and are stronger than the surrounding longitudinal field, which is less than 100 μG [64]. If the knots behaved like vortices, the vortex-twisted field lines would be amplified and have transverse components. This is, of course, only one possible explanation.

While magnetic fields tend to stabilize the system, highly relativistic flow speeds tend to have a destabilizing effect. Our numerical simulations undergo early breakdown when the unperturbed flow speed has a Lorentz factor exceeding roughly 2. In Sec. VI C, when we plotted growth rate versus wave number at highly relativistic flow speeds, we observed near-maximum growth at wavelengths which are shorter than the length scale set by the velocity shear. The highly relativistic regime also corresponds to large-amplitude spatial oscillations in the transverse profiles of the initial perturbations. These observations shed light on the early numerical breakdown of numerical viscosity simulations at high Lorentz factors.

One direction of further research is to extend the RMHD system to three dimensions and examine oblique perturbations and magnetic fields. An oblique perturbation can extract mechanical energy without performing as much work against the bulk flow. A perturbation which is oblique to the field can more easily bend the field lines. Three dimensions allow for the possibility of vortex regeneration after field-induced inhibition [38]. Magnetic field lines can also wrap around the vortex filaments whose behavior they complement [28]. Each of these possibilities would lead to a more KH-unstable system. Another possibility is to obtain results using a cylindrical geometry, and compare those to our present study. We might also compare our results to those obtained by adapting our model to high-resolution shock-capturing (HRSC) schemes, which have recently been adapted to model RMHD fluids with fairly high accuracy [54]. HRSC schemes also have the potential for modeling systems with higher Lorentz factors than those allowed by numerical viscosity schemes.

ACKNOWLEDGMENTS

We wish to thank M. G. Kivelson, F. V. Coroniti, W. B. Mori, G. Morales, R. V. E. Lovelace, P. Pritchett, R. Walker, W. Gekelman, M. Malkan, M. Morris, S. Osher, and C.-C. Wu for many useful comments and suggestions. This research was performed with the use of the Hoffman2 cluster supercomputer at the University of California, Los Angeles.

APPENDIX A: NUMERICAL SCHEME

Here, we describe the numerical algorithm for advancing the simulation forward in time. The context of this method is discussed in Sec. VII. Our method is fourth order in space and time, and numerically solves the RMHD single-fluid equations of Anile [51] in conservative form, given by (7) and (16) in diffusionless form and by (17) with numerical viscosity included. The RMHD single-fluid equations are marginally stable, but become unstable when discretized in a numerical scheme. Numerical viscosity is included in order to restore stability to the system. Diffusion is implicitly present in second order in the form of truncation error. The use of fourth-order methods in space and time therefore allows for explicit manipulation of the diffusion terms. Before describing our numerical scheme, we first make the definitions

$$w = \rho c^2 + \frac{\Gamma P}{\Gamma - 1}, \quad u^0 = \gamma, \quad u^i = \gamma \beta_i, \quad b^0 = \mathbf{B} \cdot \beta, \tag{A1}$$
$$b^i = \frac{B_i + b^0 u^i}{u^0}, \quad b_\alpha b^\alpha = b_1 b_1 + b_2 b_2 + b_3 b_3 - b_0 b_0,$$

where w is the enthalpy and Γ is the adiabatic constant. In this section, the speed of light c is normalized to unity. The

conserved quantities are then given by

$$\begin{aligned} C_1 &= \rho u^0, \\ C_2 &= (w + b_\alpha b^\alpha)u^0 u^1 - b^0 b^1, \\ C_3 &= (w + b_\alpha b^\alpha)u^0 u^2 - b^0 b^2, \\ C_4 &= (w + b_\alpha b^\alpha)u^0 u^3 - b^0 b^3, \\ C_5 &= (w + b_\alpha b^\alpha)u^0 u^0 - \left(P + \tfrac{1}{2} b_\alpha b^\alpha\right) - b^0 b^0, \\ C_6 &= B_1, \quad C_7 = B_2, \quad C_8 = B_3. \end{aligned} \tag{A2}$$

The first quantity represents mass density. The second, third, and fourth components are the components of the momentum density. The fifth component is the energy density. The sixth, seventh, and eighth components are the components of the magnetic field in the stationary frame.

We now describe the method by which we advance the simulation forward in time. We first recover the primitive variables (density, pressure, velocity, magnetic field) from the conserved quantities C_j using a highly accurate, efficient, and convergent algorithm developed by Newman [26]. We describe this algorithm in detail in Appendix B. To estimate the spatial derivatives of the flux quantities, and the second-order spatial derivatives in the diffusion terms, we use the fourth-order method of lines described in Schiesser [62], with periodic boundary conditions in both the x and z directions. We finally compute the conserved quantities at the next time step using the fourth-order Runge-Kutta method, described, for example, in Ralston and Rabinowitz [58]. Being a one-step method, the Runge-Kutta method is superior to multistep methods in several respects. It allows for more versatility in modifying such parameters as the time step. The Runge-Kutta method is also self-starting. However, one-step methods are somewhat more computationally expensive. We then repeat the above procedure at the next time step, and so on.

APPENDIX B: PRIMITIVE VARIABLE RECOVERY ALGORITHM

Here, we present the numerical relaxation scheme developed by Newman [26] for recovering the primitive variables (density, pressure, velocity, magnetic field) from the conserved quantities given by Eqs. (A2) at each time step of a simulation in relativistic magnetohydrodynamics. This method is an improvement over previous relaxation schemes, such as the Newton-Raphson method. The method of Newman [26] reduces a system of five equations [namely, the first five of Eqs. (A2)] to a single cubic polynomial in the pressure P, and is one order of magnitude faster than Newton-based methods used to solve equivalent systems. The algorithm is as follows (methods for solving the cubic equation are described in such papers as McKelvey [66] and Nickalls [67]). We first denote the momentum density, momentum density squared, and the quantity T by

$$\begin{aligned} m^i &= (w + b_\alpha b^\alpha)u^0 u^i - b^0 b^i, \\ m_\alpha m^\alpha &= C_2^2 + C_3^2 + C_4^2, \\ T^2 &= (C_2 B_2 + C_3 B_3 + C_4 B_4)^2. \end{aligned} \tag{B1}$$

We begin by making an initial guess for P, which is generally its unperturbed (equilibrium) value. We denote this P_0. We then compute

$$\begin{aligned} a &= C_5 + P_0 + \frac{B^2}{2}, \\ d &= \frac{1}{2}(m_\alpha m^\alpha B^2 - T^2). \end{aligned} \tag{B2}$$

We must now verify that P satisfies the condition

$$a \geqslant \left(\frac{27d}{4}\right)^{1/3}. \tag{B3}$$

We now make the following computations:

$$\begin{aligned} \phi &= \cos^{-1}\left[\frac{1}{a}\sqrt{\frac{27d}{4a}}\right], \\ U_1 &= \frac{a}{3} - \frac{2a}{3}\cos\left(\frac{2\phi}{3} + \frac{2\pi}{3}\right), \\ L &= U_1 - B^2, \\ \beta^2 &= \frac{m_\alpha m^\alpha L^2 - T^2(B^2 + 2L)}{L^2(B^2 + L)^2}, \\ u^0 &= \frac{1}{\sqrt{1 - \beta^2}}, \\ w &= \frac{L}{u^0 u^0}, \\ \rho &= \frac{C_1}{u^0}, \\ P_1 &= \frac{\Gamma - 1}{\Gamma}(w - \rho c^2). \end{aligned} \tag{B4}$$

We repeat this process, using P_1 as an input instead of P_0. This generates a third value P_2. We now perform convergence checks on P_0, P_1, and P_2, making sure that the magnitude of the difference between two successive estimates of P is less than a sufficiently small number of around 10^{-12}. We can then compute the Lipshitz constant R, given by

$$R = \frac{P_2 - P_1}{P_1 - P_0}. \tag{B5}$$

We then compute the Aitken accelerant P_{Aitken}, given by

$$P_{\text{Aitken}} = P_0 + \frac{P_1 - P_0}{1 - R}. \tag{B6}$$

We perform convergence checks on P_0, P_1, P_2, and P_{Aitken}. If necessary, we repeat the algorithm, using P_{Aitken} as the new P_0, and continue to do so until the convergence checks are satisfied.

The quantities P, ρ, w, β^2, u^0, and $\vec{B}$ are now known. To compute the remaining quantities, we do the following:

$$\begin{aligned} S &= \frac{T}{w u^0 u^0}, \\ \beta^i &= \frac{m^i + S B^i}{w u^0 u^0 + B^2}, \quad i = 1,2,3 \\ u^i &= \beta^i u^0, \quad i = 1,2,3. \end{aligned} \tag{B7}$$

We have at this point recovered the primitive variables (density, velocity, pressure, and magnetic field) from the conserved quantities.

[1] H. Helmholtz, Monatsberichte der Koniglichen Preussische Akademie der Wissenschaften zu Berlin **23**, 215 (1868).
[2] L. Kelvin, Philos. Mag. **42**, 362 (1871).
[3] W. Munk, J. Mar. Res. **6**, 203 (1947).
[4] J. Francis, Philos. Mag. Ser. 7, **45**, 695 (1954).
[5] S. Chandrasekhar, *Hydrodynamic and Hydromagnetic Stability* (Clarendon, Oxford, UK, 1961).
[6] K. Case, Phys. Fluids **3**, 149 (1960).
[7] F. Dyson, Phys. Fluids **3**, 155 (1960).
[8] P. Drazin, J. Fluid Mech. **4**, 214 (1958).
[9] P. Drazin and L. Howard, Adv. Appl. Mech. **9**, 1 (1966).
[10] S. Maslowe, J. Fluid Mech. **229**, 417 (1991).
[11] G. Swaters, Phys. Fluids **11**, 2546 (1999).
[12] Z.-Y. Pu and M. Kivelson, J. Geophys. Res. **88**, 841 (1983).
[13] M. Kivelson and Z.-Y. Pu, Planet. Space Sci. **32**, 1335 (1984).
[14] A. Otto and D. Fairfield, J. Geophys. Res. **105**, 21175 (2000).
[15] M. Faganello, F. Califano, and F. Pegoraro, Phys. Rev. Lett. **100**, 015001 (2008).
[16] P. Hardee, Astrophys. J. **318**, 78 (1987).
[17] P. Hardee, Astrophys. J. **597**, 798 (2003).
[18] P. Hardee, Astrophys. J. **620**, 646 (2005).
[19] A. Lobanov and J. Zensus, Science **294**, 128 (2001).
[20] B. Bicknell and M. Begelman, Astrophys. J. **467**, 597 (1996).
[21] *Superluminal Radio Sources,* edited by J. Zensus and T. Pearson (Cambridge University Press, Cambridge, UK, 1987).
[22] R. Lovelace, Nature (London) **262**, 649 (1976).
[23] R. Blandford and D. Payne, Mon. Not. R. Astron. Soc. **199**, 883 (1982).
[24] M. Rees, Nature (London) **229**, 312 (1971).
[25] N. Bucciantini and L. Del Zanna, Astron. Astrophys. **454**, 393 (2006).
[26] W. Newman (unpublished).
[27] A. Frank, T. Jones, D. Ryu, and J. Gaalaas, Astrophys. J. **460**, 777 (1996).
[28] D. Ryu, T. Jones, and A. Frank, Astrophys. J. **545**, 475 (2000).
[29] H. Baty, R. Keppens, and P. Comte, Phys. Plasmas **10**, 4661 (2003).
[30] A. Ferrari, E. Trussoni, and L. Zaninetti, Mon. Not. R. Astron. Soc. **193**, 469 (1980).
[31] G. Bodo, A. Mignone, and R. Rosner, Phys. Rev. E **70**, 036304 (2004).
[32] W. Blumen, J. Fluid Mech. **40**, 769 (1970).
[33] W. Blumen, P. Drazin, and D. Billings, J. Fluid Mech. **71**, 305 (1975).
[34] T. Ray, Mon. Not. R. Astron. Soc. **198**, 617 (1982).
[35] M. Birkinshaw, Mon. Not. R. Astron. Soc. **252**, 505 (1991).
[36] A. Miura and P. Pritchett, J. Geophys. Res. **87**, 7431 (1982).
[37] S. Choudhury and R. Lovelace, Astrophys. J. **302**, 188 (1986).
[38] A. Malagoli, G. Bodo, and R. Rosner, Astrophys. J. **456**, 708 (1996).
[39] R. Keppens, G. Tóth, R. Westermann, and J. Goedbloed, J. Plasma Phys. **61**, 1 (1999).
[40] G. Duncan and P. Hughes, Astrophys. J. Lett. **436**, L119 (1994).
[41] J. Marti, E. Muller, J. Font, and J. Ibanez, Astrophys. J. **448**, L105 (1995).
[42] S. Koide, K.-I. Nishikawa, and R. Mutel, Astrophys. J. **463**, L71 (1996).
[43] T. Leismann, L. Anton, M. Aloy, E. Muller, J. Marti, J. Miralles, and J. M. Ibanez, Astron. Astrophys. **436**, 503 (2005).
[44] A. Mignone, P. Rossi, G. Bodo, A. Ferrari, and S. Massaglia, Mon. Not. R. Astron. Soc. **402**, 7 (2010).
[45] W. Bickley, Philos. Mag. **23**, 727 (1937).
[46] P. Savic, Philos. Mag. **32**, 245 (1941).
[47] F. Lipps, J. Fluid Mech. **12**, 397 (1962).
[48] M. Stern, Tellus **13**, 503 (1961).
[49] G. Mattingly and W. Criminale, J. Fluid Mech. **51**, 233 (1972).
[50] L. Howard and P. Drazin, J. Math. Phys. **43**, 83 (1964).
[51] A. Anile, *Relativistic Fluids and Magneto-fluids* (Cambridge University Press, Cambridge, UK, 1989).
[52] S. Komissarov, Mon. Not. R. Astron. Soc. **303**, 343 (1999).
[53] D. Balsara, Astrophys. J., Suppl. Ser. **132**, 83 (2001).
[54] A. Mignone, M. Ugliano, and G. Bodo, Mon. Not. R. Astron. Soc. **393**, 1141 (2009).
[55] J. Zrake and A. MacFadyen, Astrophys. J. **744**, 32 (2012).
[56] R. Lovelace, M. Romanova, and W. Newman, Mon. Not. R. Astron. Soc. **402**, 2575 (2009).
[57] E. Hairer, S. Norsett, and G. Wanner, *Solving Ordinary Differential Equations I: Nonstiff Problems*, Second Revised Edition, Chap. 1 (Springer-Verlag, Berlin, 2000), pp. 105–110.
[58] A. Ralston and P. Rabinowitz, *A First Course in Numerical Analysis* (Dover, New York, 2001).
[59] J. Marti and E. Muller, Living Rev. Relativity **6**, 7 (2003).
[60] K. Lang, *Astrophysical Formulae. Vol. 2. Space, Time, Matter and Cosmology* (Springer, New York, 1999).
[61] A. Simon, Phys. Rev. **100**, 1557 (1955).
[62] W. Schiesser, *The Numerical Method of Lines: Integration of Partial Differential Equations* (Academic, New York, 1991).
[63] N. Hamlin, Ph.D. dissertation, University of California, Los Angeles, 2012.
[64] D. Hines, F. Owen, and J. Eilek, Astrophys. J. **347**, 713 (1989).
[65] L. Stawarz, A. Siemiginowska, M. Ostrowski, and M. Sikora, Astrophys. J. **626**, 120 (2005).
[66] J. McKelvey, Am. J. Phys. **52**, 269 (1984).
[67] R. Nickalls, Math. Gazette, **77**, 354 (1993).